doi:10.1038/nature10374

Contents

1 Observations and Data Analysis

1.1 *Swift* Discovery and Observations

Here we provide more detail on the *Swift* discovery and observations of the source, Swift J164449.3+573451.

1.1.1 BAT Observations

The discovery of Swift J164449.3+573451 is discussed in this section.

The *Swift*[31] Burst Alert Telescope[32] (BAT, 15-150 keV) triggered on 28 March 2011 at 13:18 UT on a new uncatalogued source in a 1208 s Image Trigger beginning at $T_0 = 12{:}57{:}45$ UT[33]. The source was assumed to be a γ-ray burst (GRB) and was named GRB 110328A, following standard nomenclature. However, this trigger was followed by three additional BAT triggers at increasing count rates over the next two days[34] (see Supplementary Table 1), making it clear that this object was not, in fact, a GRB. (Following the fourth trigger, the on-board BAT source catalog was adjusted to prevent further triggers.) The source was renamed Swift J164449.3+573451, which is now the preferred name of the source[35], based on the initial position of the X-ray counterpart. We will refer to Swift J164449.3+573451 as Sw J1644+57 for the remainder of this paper.

Post-facto examination of pre-trigger data indicates that the outburst was first detected by BAT on 25 March 2011 with a mean count rate (integrated over 24 hours) of (0.0059 ± 0.0016) counts cm^{-2} s^{-1} (too low to generate an on-board trigger) and with peak BAT count rates of ~ 0.02 counts cm^{-2} s^{-1} during the days prior to the on-board trigger. We note that the source was outside the BAT FOV for 2.86 hours before the first trigger. Between 28 March and 31 March the BAT data show multiple flares peaking at up to 0.09 counts cm^{-2} s^{-1} (about 22 mCrabs). During the

Supplementary Table 1 | *Swift* BAT Trigger Details for Sw J1644+57.

Trigger Number	Date	Trigger Start Time (UT)	Trigger Duration (s)	Intensity (counts s^{-1})
450158	28 Mar	12:57:45	1208	6.1
450161	28 Mar	13:40:41	64	19.4
Threshold set to 0 so BAT would trigger on Sw J1644+57 again				
450257	29 Mar	18:26:25	320	15.6
450258	29 Mar	19:57:45	64	38.2
Triggers from Sw J1644+57 disabled				

brightest parts of the outburst, the source had power law photon indices ranging from 1.3 to 1.8. The average 15-150 keV flux in the time interval 12:57:45 UT on 28 March 2011 to 05:30 UT on 30 March 2011 was about $(1.0 \pm 0.2) \times 10^{-9}$ erg cm^{-2} s^{-1}. The source flux then dropped dramatically, with an average count rate of 0.0020 ± 0.0005 counts cm^{-2} s^{-1} between 2 April 2011 and 12 April 2011 (see Supplementary Figure 1). Sw J1644+57 was still being detected by the BAT in one-day integrations at a flux of about 5 mCrabs through the beginning of June 2011.

For most of the BAT data the spectral slope cannot be determined, making it difficult to determine an accurate flux based on the count rates. However if we assume a spectral slope, we can obtain estimates of the 15 – 150 keV flux. Supplementary Table 2 provides flux conversions for average BAT count rates at 3 epochs, for 2 observed spectral slopes that cover the range observed during the brightest flares.

Supplementary Table 2 | Flux Conversion for Observed BAT Count Rates for Different Spectral Slopes

Time Period	BAT count rate (cts s^{-1} cm^{-2})	Photon Index (assumed)	Estimated Flux (erg cm^{-2} s^{-1}, 15-150 keV)
Pre-Trigger	0.0059	1.8	5.1×10^{-10}
	0.0059	1.3	6.1×10^{-10}
Peak rate	0.0900	1.8	7.8×10^{-9}
	0.0900	1.3	9.3×10^{-9}
Late time	0.0020	1.8	1.7×10^{-10}
	0.0020	1.3	2.1×10^{-10}

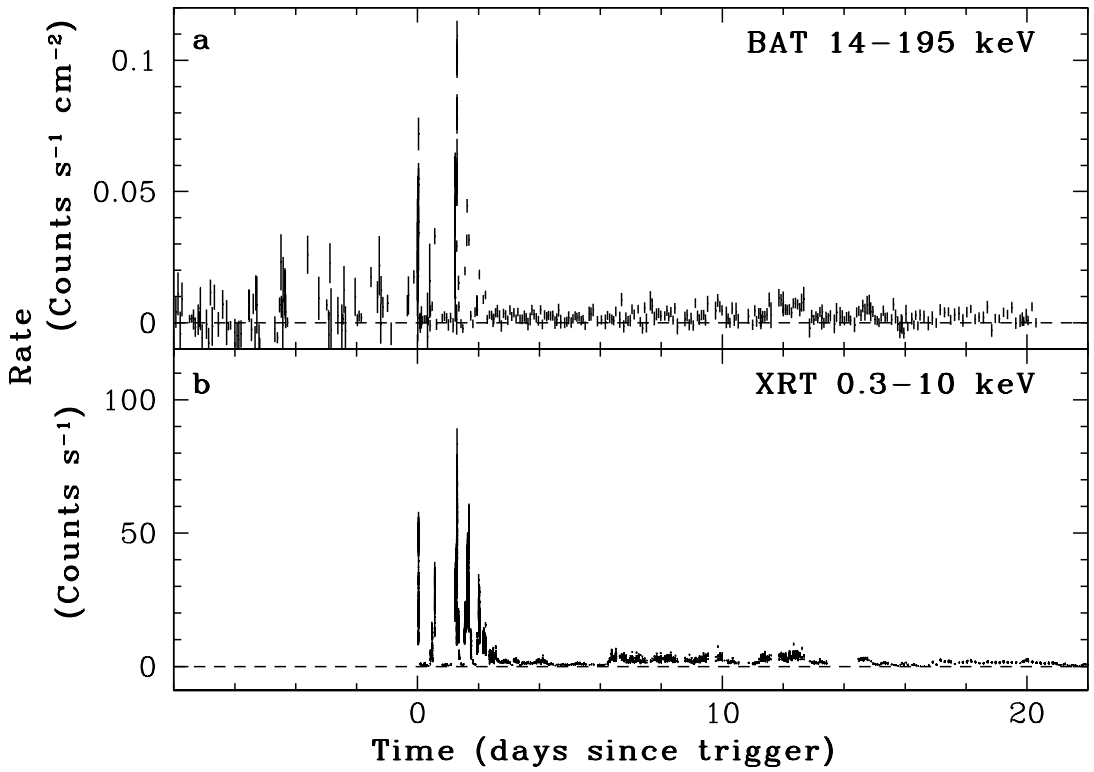

Supplementary Figure 1 | BAT and XRT light curves of Sw J1644+57for the first 3 weeks. a) BAT light curve, beginning 5 days before the first on-board BAT trigger. b) XRT light curve. XRT data begin following the first BAT on-board trigger. Times are measured from the first BAT trigger on 28 March 2011. The count rates in both instruments track each other, with numerous flares in the first few days after the BAT trigger. Note that Sw J1644+57 was detected by BAT ~ 3.5 days before BAT triggered and XRT observations began. Although not shown here, Sw J1644+57 was still being detected by the BAT through the beginning of June 2011. BAT error bars are larger pre-trigger because Sw J1644+57 was being observed off-axis. Data gaps are caused by periods when the source was not being observed.

1.1.2 XRT Observations

Following the discovery of Sw J1644+57 by the *Swift* BAT instrument, the spacecraft automatically slewed to point its narrow field instruments towards the source. Observations of Sw J1644+57 with the *Swift* X-ray Telescope[36] (XRT, 0.3 – 10 keV) began at 13:20:52 UT on 28 March 2011, 245 s after the BAT software found the source position. XRT observed Sw J1644+57 daily for up to 28 ks per day. The mean time spent on-target during the first 50 days was 12.4 ks per day. Because *Swift* is in a low-Earth orbit, observations are broken into small snapshots, typically 20 – 30 min long per ~ 96 min *Swift* orbit. This produces regularly spaced data gaps.

We report here on the first ~ 100 days after the initial BAT trigger. For the first 14.5 days the XRT was in "Auto State", in which it autonomously selects the appropriate observing mode based upon the brightness of the observed source. As the source varied in brightness, the XRT collected data in a combination of Windowed Timing (WT) and Photon Counting (PC) modes. PC mode is the standard XRT imaging mode, with a time resolution of 2.5 s; if a source is brighter than ~ 0.5 XRT count s^{-1} in this mode, photons pile up (saturate) and special processing techniques must be used to obtain accurate fluxes and spectral fits from the wings of the Point Spread Function[37]. WT mode is a fast timing mode that collects 1-dimensional image data with 1.8 ms time resolution. The fast readout of WT mode means that pile-up is avoided for sources with a count rate below ~ 100 counts s^{-1}.

The switch points for Auto State are tuned specifically for GRB observations, i.e. a fading X-ray light curve. For much of the second and third weeks after the trigger, Sw J1644+57 was at moderate brightness (1-5 XRT counts s^{-1}) with data being collected in PC mode, and these data are severely piled-up. We changed our observing mode to WT for data collected from 12 April 2011 until 07 May 2011, when the typical count rate had decreased enough to return to PC mode.

X-ray spectra and light curves were produced utilising the methods described by Evans et al.[38] All PC mode data were corrected for pile-up by removing events from the core of the PSF, and utilising the wings of the PSF for both spectral fitting and light curve generation[37]. XRT spectra were corrected for the effects of charge traps that have developed due to radiation damage to the CCD over the *Swift* mission lifetime[39].

The XRT count rate light curve for Sw J1644+57 is shown in Supplementary Figures 2 and 3. Total exposure time for the first 50 days is 6.1×10^5 s, with a mean duty cycle of 14.3%. The X-ray light curve is complex, but can be roughly described after the first week as an exponentially decreasing flux with an e-folding time of 27 days, punctuated at irregular intervals by deep dips in which the flux drops by factors of 3 – 10. (During the first 50 days, the light curve is also roughly consistent with a $t^{-5/3}$ power law.) However, the gradual decay can also be described as plateaus lasting for days or weeks, punctuated by dips and separated by downward steps in flux, or at episodes of flaring (which are more prominent when plotted in linear axes as in Supplementary Figure 1). Longer-term monitoring may help distinguish the true shape/characterization of the light curve.

We produced light curves in two energy bands (soft and hard) in order to examine spectral variations with time and flux. During the first few weeks, we find a strong anti-correlation in WT mode data between the spectral hardness and flux, with softer spectra as the source intensity decreases (see Supplementary Figure 4). There is a similar correlation in PC mode data, but the scatter is larger and the correlation is weaker.

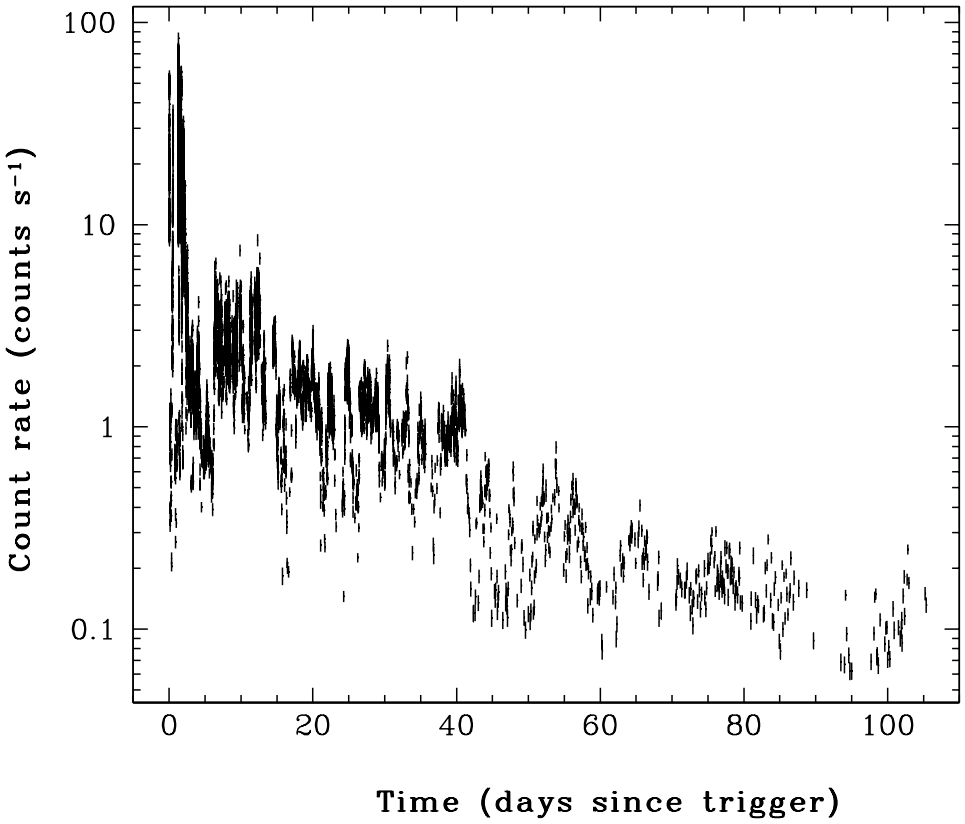

Supplementary Figure 2 | *Swift* XRT count rate light curve of Sw J1644+57, through 13 July 2011. Following nearly 3 days of intense flaring with peak count rates of over 80 counts s^{-1}, the source decayed for several days to a count rate of about 0.7 counts s^{-1}, then rose to $\sim$2–3 counts s^{-1}, where it remained (with excursions) for over 9 days. The count rate then began a slow, roughly exponential decline with episodes of dipping lasting $1-2$ days, during which the count rate drops by a factor of 5–10 and then recovers to the pre-dip level.

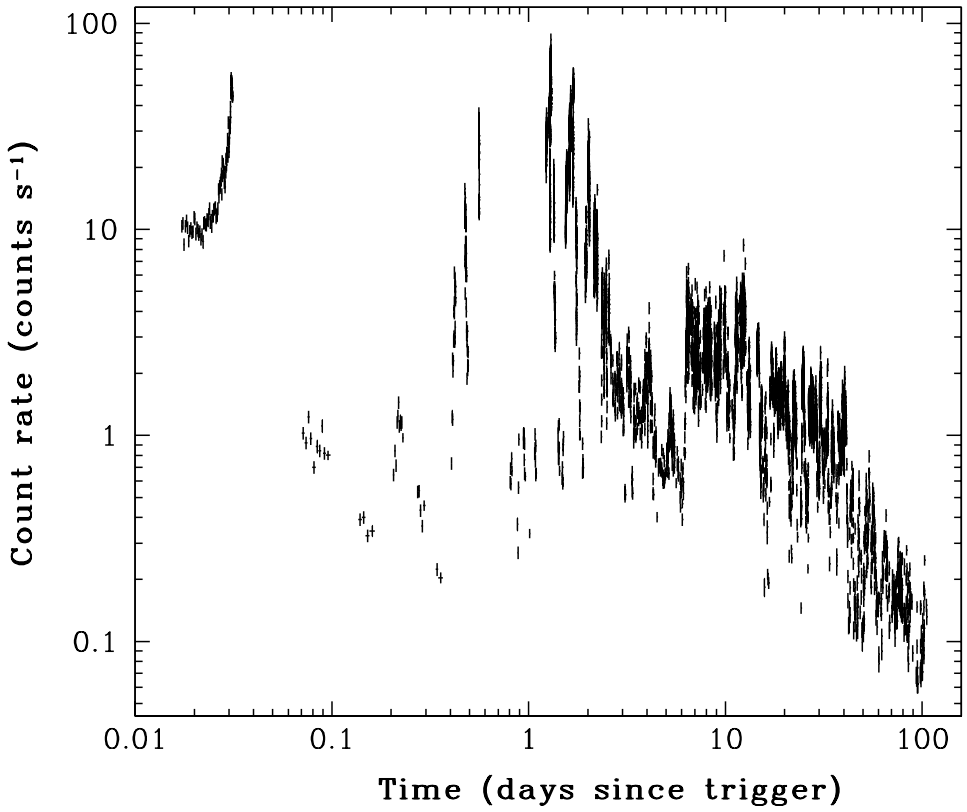

Supplementary Figure 3 | *Swift* XRT count rate light curve of Sw J1644+57, through 13 July 2011. Same as previous figure, but on log-log scale.

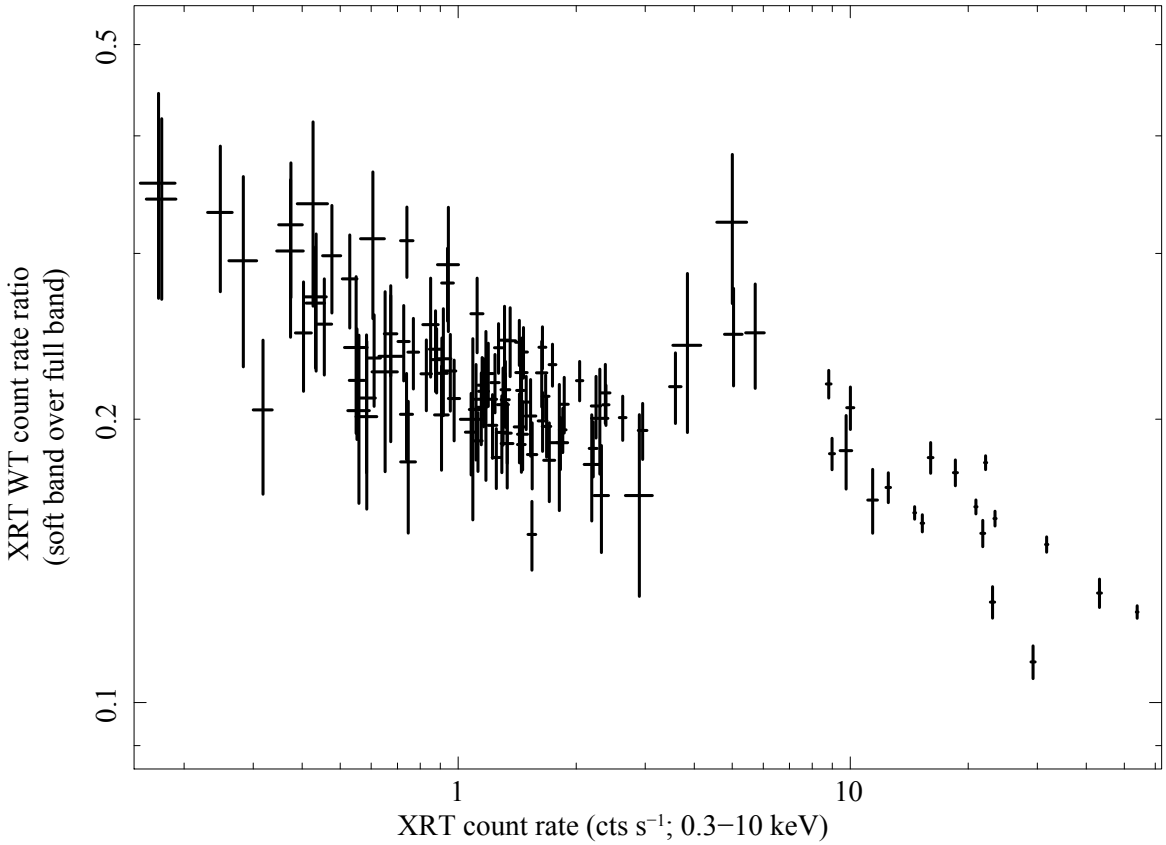

Supplementary Figure 4 | Ratio of XRT count rates in the 0.3 – 1.3 keV and 0.3 – 10 keV bands, plotted against the overall XRT count rate. The band ratio is strongly correlated with the overall count rate, demonstrating that the spectrum gets progressively harder as the flux increases. There is a discontinuity around 4 ct/s; data at higher count rates were collected during flares in the first few days of monitoring, whilst data at lower count rates were collected after the XRT observing mode was changed from Auto to WT 14.5 days after the first BAT trigger. The trend for harder spectra at higher count rates is seen on both sides of this discontinuity. This figure includes only WT-mode data taken within 23 days of the first BAT trigger. Each data point averages all WT data collected within a single *Swift* orbit. Only data points with uncertainties smaller than 25% are shown.

1.1.3 UVOT Observations

The *Swift* UV-Optical Telescope[40] (UVOT) observed Sw J1644+57 in all optical and ultraviolet filters immediately following each of the four *Swift* BAT triggers. Followup observations have been conducted by cycling through the UVOT u band and UV filters, one per day, with observations in UVOT white band every few weeks. Observing periods are the same as for XRT. A persistent source is detected in the white band at the location of Sw J1644+57 (peak significance $\sim 5\sigma$), and a marginal (3σ) source detection in u was obtained during the first few days after the BAT triggers (Supplementary Table 3).

Photometry was performed using the UVOT photometric system[41]. Source counts were extracted using a 2.5″ aperture, a 25″ concentric background region with other sources removed, and an aperture correction using the curve-of-growth model available in the *Swift* UVOT FTOOLs. No correction has been applied for Galactic extinction due to the reddening of E(B-V) = 0.02 in the direction of the transient[42]. No attempt has been made to subtract the host galaxy contribution from the individual measurements reported in Supplementary Table 3, which provides the results for five epochs: two epochs during the early X-ray variability and three, successive three-week periods. Exposures are in seconds; upper limits are 3σ.

The UVOT white filter is a clear filter with a broad spectral response centred on 385 nm with FWHM = 260.0 nm, whilst the UVOT u filter is centred on 345 nm with FWHM = 87.5 nm. Whilst the first white band measurement, taken during the bright X-ray flares, is slightly brighter than the later ones, all five measurements are statistically consistent with a constant source. Combining the late-time observations gives a mean brightness of 24.2 ± 0.2 magnitudes in the white band. The first observation is brighter than this value with 2.1σ significance. The significance is too low to claim a detection of the transient.

Supplementary Table 3 | UVOT UV & Optical Photometry

	T_0+0-2 days		$3-5$ days		$6-26$ days		$27-45$ days		$46-70$ days	
Filter	Exp (s)	Mag	Exp (s)	Mag	Exp (s)	Mag	Exp (s)	Mag	Exp (s)	Mag
wh	18358	23.6±0.2	11221	24.1±0.4	*no observations*		30287	24.2±0.3	28271	24.3±0.3
v	2541	>21.8	*no observations*							
b	1493	>22.2	*no observations*							
u	31593	23.6±0.4	11412	>23.3	70908	>24.0	40094	>23.8	59803	>24.2
w1	3422	>22.4	38863	>23.8	66579	>24.0	47759	>23.9	37589	>23.8
m2	3048	>22.2	*no observations*		84371	>24.0	28736	>23.6	49958	>23.9
w2	2320	>22.4	*no observations*		54222	>24.2	31016	>23.8	53197	>24.3

1.2 Ground-based Optical/NIR Observations

Sw J1644+57 has been observed by a large number of ground-based optical and radio telescopes. In general, the heavily extincted optical counterpart is not clearly detected in optical or UV bands, where the host galaxy dominates the light, but is detected strongly in the near-infrared. Spectroscopic observations identified emission lines at a redshift of 0.354[43]. Here we report details of optical and NIR observations obtained by our team. These observations are used to measure the spectral energy distribution of the source, which constrains models of the emission mechanisms (SI§2.3).

1.2.1 R-band Observations

R-band imaging data were taken using a CCD camera on the Mt. Lemmon Optical Astronomy Observatory (LOAO) 1-m telescope[44,45] in Arizona, USA, and SNUCAM[46] on the Maidanak Observatory 1.5-m telescope in Uzbekistan. The data were taken during the nights of 29 March 2011 to 8 April 2011 at LOAO, and 12 April at Maidanak. A dithered sequence of 300 s – 600 s exposures were taken, resulting in 20 min – 1 hour total integration for each night, which gave 3σ detection limits of $R = 22.4 - 23.9$ mag over a $3''$ diameter aperture. The photometric calibration is based on field calibration performed using four Landolt standard star fields (PG1633+099, SA110, SA107 and PG1657+078) by the Lulin One-meter Telescope operated by National Central University. The summary of our observations and results are in Supplementary Table 4.

Supplementary Table 4 | Log of R-band Observations of Sw J1644+57.

Start(UT)	End(UT)	Time(Mid Time) (UT)	Filter	Exp(s)	Magnitude
LOAO:					
2011-03-29T10:53:45	2011-03-29T10:59:51	2011-03-29T10:56:48	R	300×5	22.45 ± 0.49
2011-03-30T10:50:24	2011-03-30T11:47:47	2011-03-30T11:19:06	R	300×12	22.33 ± 0.22
2011-04-05T11:15:26	2011-04-05T12:02:33	2011-04-05T11:39:00	R	300×6	22.35 ± 0.25
2011-04-06T11:18:05	2011-04-06T12:22:00	2011-04-06T11:50:03	R	300×12	22.20 ± 0.31
2011-04-08T10:09:28	2011-04-08T11:29:07	2011-04-08T10:49:17	R	300×14	22.73 ± 0.26
Maidanak Obervatory:					
2011-04-12T22:49:39	2011-04-12T23:10:21	2011-04-12T22:59:59	R	600 × 2	22.49 ± 0.12

1.2.2 NIR Observations and Data Analysis

We imaged the field of Sw J1644+57 with the Korea Astronomy and Space science Institute (KASI) Near Infrared Camera System (KASINICS[47]) on the 1.8m telescope at the Bohyunsan Optical Astronomy Observatory (BOAO) in Korea; with the NICS camera[48] on the Italian 3.6m Telescopio Nazionale Galileo (TNG), located in La Palma, Canary Islands; with the 3.8m United Kingdom Infrared Telescope (UKIRT) on Mauna Kea, Hawaii; and with the 3.6m Canada-France-Hawaii Telescope (CFHT) on Mauna Kea. Near-Infrared J, H and K/Ks-band observations were carried out between 30 March 2011 and 11 June 2011. Most nights were clear, with seeing in the range $0.7'' - 1.5''$. The complete observing log is reported in Supplementary Table 5.

The KASINICS images were reduced using the *xdimsum* package of IRAF. For the TNG data, image reduction was carried out using the jitter pipeline data reduction, part of the ESO-Eclipse package. The UKIRT data were reduced at the Cambridge Astronomy Survey Unit (CASU) using their standard WFCAM pipeline (*http://casu.ast.cam.ac.uk*). The CFHT data were reduced by the standard WIRCam pipeline (*http://www.cfht.hawaii.edu/Instruments/Imaging/WIRCam/*) and the stacking of WIRCam images was performed with *swarp* (*http://www.astromatic.net/software/swarp*). Following initial data reduction, all of the NIR data were analyzed in the same way. Astrometry was performed using the 2MASS (*http://www.ipach.caltech.edu/2mass*) catalogue. Aperture photometry was made with the *photom* tool implemented in the GAIA package and the DAOPHOT package[49], and the photometric calibration to the *Ks* band was done

Supplementary Table 5 | Near Infrared Observing Log

Time of obs (UT)	$T - T_0$ (days)	Telescope	Inst	Filter	Exp (s)	Magnitude
2011-03-30.650910	2.11081	BOAO	KASINICS	K_s	120×43	16.78 ± 0.07
2011-03-31.23164	2.69558	TNG	NICS	K	20×3×40	16.93 ± 0.04
2011-03-31.636350	3.09625	BOAO	KASINICS	K_s	90×32	17.07 ± 0.08
2011-03-31.67763	3.13753	BOAO	KASINICS	H	60×48	18.44 ± 0.09
2011-04-02.13674	4.59748	TNG	NICS	J	60×1×40	20.10 ± 0.12
2011-04-02.17847	4.63973	TNG	NICS	H	20×3×40	19.12 ± 0.09
2011-04-02.22289	4.68682	TNG	NICS	K	20×3×40	17.77 ± 0.10
2011-04-03.648840	6.10874	BOAO	KASINICS	K_s	60×64	18.09 ± 0.11
2011-04-03.689630	6.14953	BOAO	KASINICS	H	60×96	19.06 ± 0.11
2011-04-13.12765	15.59158	TNG	NICS	K	20×3×20	18.24 ± 0.14
2011-04-13.98145	16.44759	TNG	NICS	K	20×3×40	18.34 ± 0.10
2011-04-21.628970	24.08887	UKIRT	WFCAM	K	10×144	18.243 ± 0.038
2011-04-21.927812	24.40270	TNG	NICS	K	20×3×60	18.22 ± 0.10
2011-04-24.654872	27.11477	BOAO	KASINICS	K_s	90×23	17.75 ± 0.22
2011-04-26.576100	29.03600	UKIRT	WFCAM	K	10×144	17.984 ± 0.029
2011-04-26.592014	29.05191	UKIRT	WFCAM	J	20×72	20.302 ± 0.081
2011-04-27.527095	29.98700	UKIRT	WFCAM	H	10×144	19.168 ± 0.101
2011-04-27.548345	30.00824	UKIRT	WFCAM	K	10×144	18.088 ± 0.066
2011-04-28.620544	31.08044	UKIRT	WFCAM	H	10×72	19.234 ± 0.077
2011-04-28.631273	31.09117	UKIRT	WFCAM	K	10×72	18.22 ± 0.07
2011-04-28.734571	31.19447	BOAO	KASINICS	K_s	90×130	18.14 ± 0.09
2011-04-29.515498	31.97539	UKIRT	WFCAM	K	10×72	18.095 ± 0.044
2011-04-30.520787	32.98068	UKIRT	WFCAM	H	10×72	19.191 ± 0.067
2011-04-30.531690	32.99159	UKIRT	WFCAM	K	10×72	18.18 ± 0.05
2011-05-03.215486	35.67539	TNG	NICS	K	20×3×60	18.22 ± 0.05
2011-05-19.364105	51.82407	CFHT	WIRCam	K_s	20×96	18.306 ±0.054
2011-06-04.431019	67.89091	UKIRT	WFCAM	K	10×144	18.45 ± 0.05
2011-06-07.912083	71.37198	TNG	NICS	K	20×3×60	18.59 ± 0.09
2011-06-11.018148	74.47805	TNG	NICS	K	20×3×60	18.70 ± 0.08

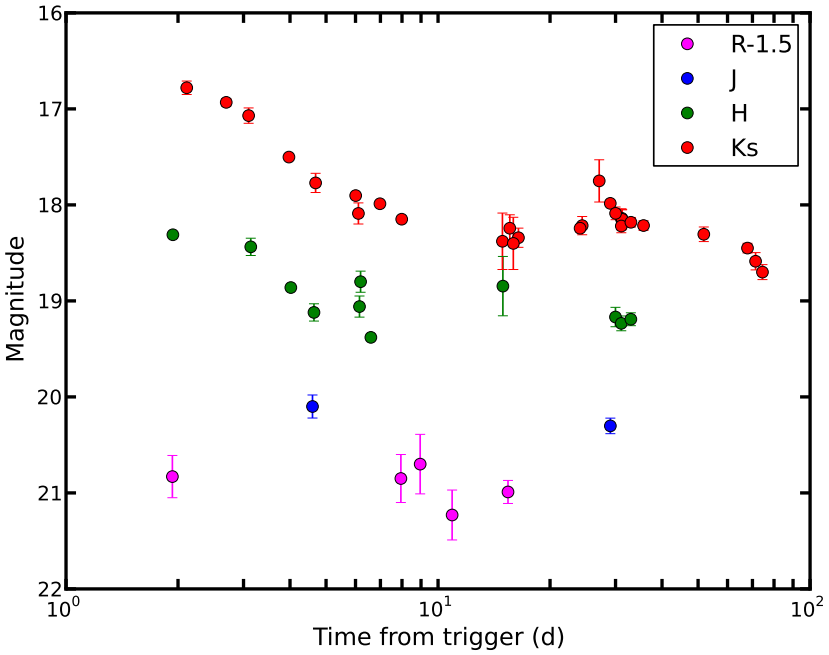

Supplementary Figure 5 | Optical/NIR light curves in the R (magenta), J (blue), H (green) and Ks (red) bands of Sw J1644+57. No variability has been detected in the R band whilst in the NIR a decay trend roughly consistent with X-ray data is visible. Error bars are 1σ.

against the 2MASS catalogue. In order to minimize any systematic effect, we performed differential photometry with respect to a selection of local, isolated and unsaturated reference stars visible in the field of view.

The *Swift* XRT light-curve (Supplementary Figure 2) shows strong variability at essentially every epoch, superposed on a general long-term flux decrease. A similar overall behaviour is seen in the NIR band, although not strictly correlated with the one seen in the X rays. The maximum NIR flux is observed at about 2 days after the first *Swift* trigger (see Supplementary Figure 5), followed by a global flux decrease. A rather stable phase begins after about a week with some "flaring" activity observed at around day 27 (after the first BAT trigger). At more than two months after the trigger the NIR light-curve shows another rapid decay implying that the NIR emission is still dominated by the transient and not by the host galaxy.

1.2.3 Extinction Measurement

By means of almost simultaneous z, J, H, K, and L observations (combining our data with those of Levan et al.[43]) in the first days after the *Swift* trigger when the transient was brighter, we can use the SED of the transient to evaluate the presence of substantial rest-frame extinction. Modeling the SED with a power-law in frequency we find that solutions with a rather flat or even increasing spectrum are favored ($\nu^{\sim 1/3}$). The required extinction, assuming a Milky Way extinction curve[50], is in the range $E_{B-V} \sim 1-3$, with a strong covariance with the spectral index, and is consistent with the observed near-constancy of the R-band flux. The R-band emission is dominated by the galaxy, which was already detected before the transient event[51], whilst the transient contribution is depressed well below the host-galaxy brightness by local intrinsic absorption. In order to obtain a consistent broad-band SED, we assumed $E_{B-V} = 1.5$ ($A_V = 4.5$) in subsequent analysis (see SI§2.3).

1.3 Observations by other X-ray/γ-ray Observatories

1.3.1 *MAXI*

Following the BAT on-board trigger, the *MAXI*[52] team reported that the Gas Slit Camera[53] also detected Sw J1644+57[54]. The source rises to a peak about a day after the first BAT trigger. *MAXI* continued to detect the source for the initial bright flaring part of the outburst. The *MAXI* one-day-averaged light curve for the period before and after the first BAT trigger is shown in Supplementary Figure 6.

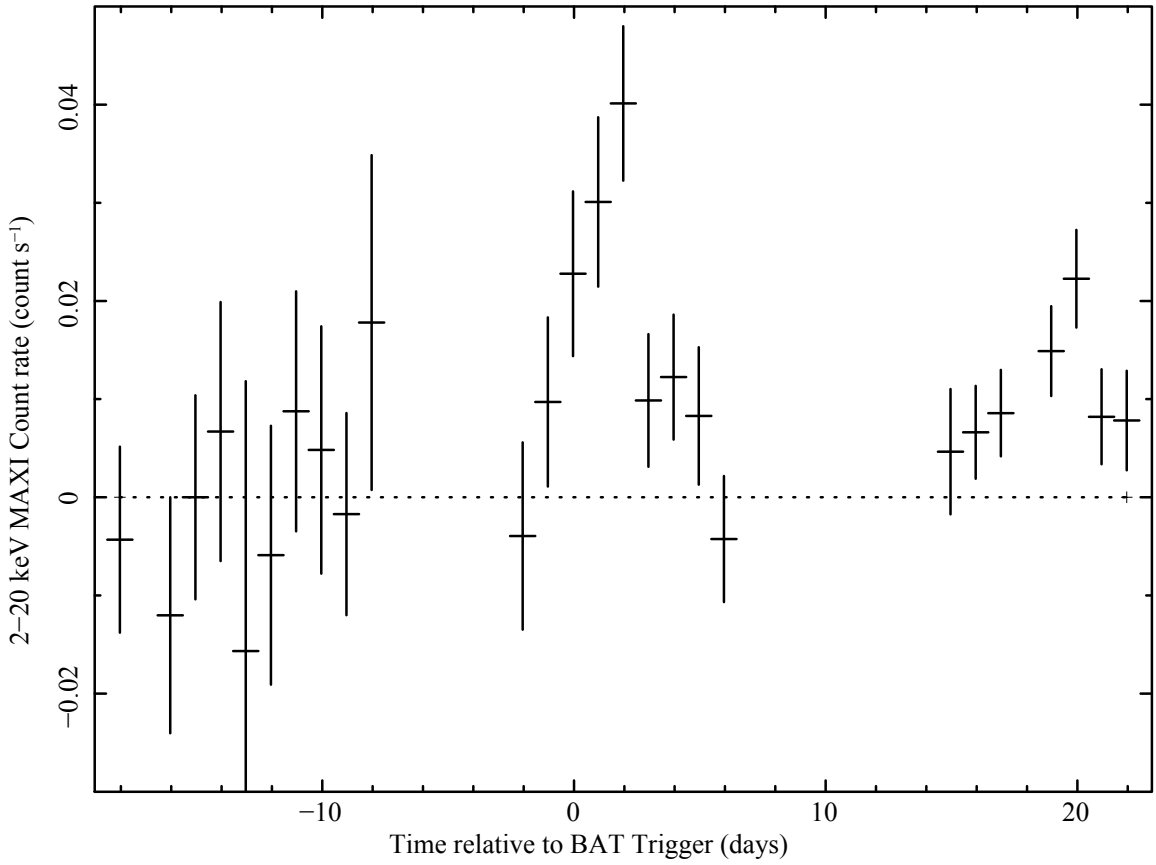

Supplementary Figure 6 | *MAXI* one-day-averaged light curve covering the ∼20 days before and after the detection of Sw J1644+57 by BAT.

1.3.2 *Fermi*

In the GeV energy range, no significant γ-ray emission has been seen by the *Fermi* Large Area Telescope (LAT) from the direction of Sw J1644+57. During the period of main activity (28 March to 4 April 2011) *Fermi* LAT observations constrain the average γ-ray flux to $< 2.7 \times 10^{-11}$ erg cm^{-2} s^{-1} (100 MeV-10 GeV, 95% confidence upper limit). During the following week, the equivalent upper limit is 2.9×10^{-11} erg cm^{-2} s^{-1}. The LAT analysis was performed with the "DIFFUSE" event class and the Pass 6, v3 (P6_V3_DIFFUSE) version of the instrument response functions. In our analysis, we modeled the background from both the Galactic diffuse emission and the corresponding spectrum of the isotropic emission, including residual background from cosmic rays misclassified as γ-rays (both available at the FSSC web site). There are no bright γ-ray sources in the proximity of Sw J1644+57; therefore no additional point sources have been added to our background model. Upper limits were derived by modeling a point source at the position of Sw J1644+57, with a spectrum described by a power law with a fixed photon index (Γ=2.5).

Supplementary Figure 7 shows the daily upper limits during the period between 17 March 2011 and 8 April 2011, corresponding to the X-ray outburst activities. For the daily upper limits we used only the isotropic background component, which is the only significant component over this time scale. No significant detection or variation of the background is observed in this time period.

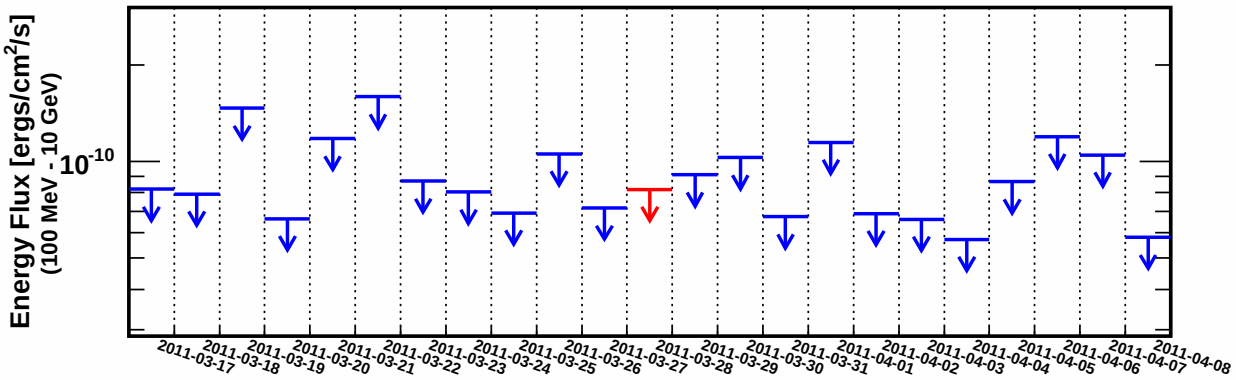

Supplementary Figure 7 | *Fermi* 95% confidence upper limit light curve of Sw J1644+57 for the period 17 March 2011 to 8 April 2011. The red upper limit is for the day of the first BAT trigger.

1.4 X-ray Variability and Timing Analysis

The X-ray flux from Sw J1644+57 is highly variable on time-scales as short as tens of seconds. Details of some of the bright flares during the first few days after the first BAT trigger are shown in Supplementary Figure 8, and measures of some of the steepest flux changes are given in Supplementary Table 6. Here t_1 and t_2 are the centres of two time bins, R_1 and R_2 are the count rates in those bins, $\sigma_{R,1}$ and $\sigma_{R,2}$ are the uncertainties in the count rates, ΔT is the time difference between the two rate measurements, ΔR and $\sigma_{\Delta R}$ are the difference in count rates and the uncertainty in that difference. The last two columns in Supplementary Table 6 give the percentage increase in count rate between the two time bins, and the significance of the rate change.

Supplementary Table 6 | Early XRT Count Rate Variability (0.3 – 10 keV)

Suppl. Fig.	t_1 (s)	R_1 (cps)	$\sigma_{R,1}$ (cps)	t_2 (s)	R_2 (cps)	$\sigma_{R,2}$ (cps)	ΔT (s)	ΔR (cps)	$\sigma_{\Delta R}$ (cps)	Rate Increase	$\#\sigma$
8a	2638.9	35.7	1.7	2649.7	48.9	2.3	10.8	13.2	2.9	37%	4.6
8b	48483.7	12.5	0.6	48512.2	21.8	1.0	28.5	9.3	1.2	74%	7.7
8c	110995.7	9.0	0.5	111027.8	14.7	0.7	32.1	5.7	0.9	64%	6.5
8c	111420.7	8.6	0.6	111495.5	25.3	1.2	74.8	16.7	1.3	194%	12.7
8c	112214.4	55.0	2.7	112249.8	73.0	3.5	35.4	18.0	4.4	33%	4.1
8d	145766.9	28.8	1.4	145834.6	48.8	2.3	67.7	20.0	2.7	69%	7.5
8d	145783.7	30.9	1.5	145834.6	48.8	2.3	50.9	17.9	2.7	58%	6.5
8d	145799.3	34.3	1.7	145834.6	48.8	2.3	35.3	14.5	2.8	42%	5.1

We note that the count rate changes by as much as 37% (4.6σ) in as short an interval as 10.8 s, and nearly triples (with 12.7σ significance) in as short an interval as 74.8 s. Such rapid variability places strong constraints on the size of the emitting volume (by speed of light arguments) unless the jet structure itself causes short time-scale variability. We have searched the light curve for the minimum 3σ doubling time, taking the conservative approach that the time interval is taken from the beginning of the first time bin to the end of the last time bin (whereas the time intervals in Supplementary Table 6 are taken from the central points of each time bin). We find that a conservative limit on the 3σ doubling time is 107 s, which we use in SI§2.1 to derive a limit on the mass of the black hole.

We have examined the XRT data to search for periodic signals that might give hints on the nature of the emission. After applying the barycentric correction to the XRT event lists we searched for coherent or quasi-periodic signals over different energy ranges and time intervals by using Fourier techniques. Due to the presence of strong non-Poissonian noise, mainly introduced by the rapid variability of the source, particular care must be taken in evaluating the statistical significance of any candidate signal. Following the prescriptions of Israel & Stella[55], no significant (periodic or quasi-periodic) signal was found. We report here upper limits on the pulsed fraction, defined as semi-amplitude of the sinusoid divided by the mean source count rate, computed for data in the time interval from 31 March 2011 to 19 April 2011 and over the energy range $0.3-10$ keV. We excluded the initial intense flares during the first few days after the first BAT trigger in order to mitigate low frequency noise in the power spectrum. We executed 524,288 trials between 1×10^{-6} and 0.2 Hz, and obtained conservative 3σ upper limits in the 1%-3% range for periods shorter than 500 s, and in the 5%-90% range for periods between $\sim$500 s and 1000 s. To summarize, we find no periodic signals that could be produced by either spin of a central object or orbital periods. We also find no statistically significant evidence for quasi-period oscillations such as those seen in Galactic stellar-mass black hole systems. These results are consistent with our conclusion that Sw J1644+57 is produced by accretion onto a supermassive black hole.

We also checked for the possible presence of a periodic component in the peaks and dips of the late-time light curve. This was performed in several different ways: by simply fitting the light curve with a sinusoidal model, by looking for significant peaks in the de-trended power spectrum, and through a Rayleigh periodogram. These analyses suggest the presence of a recurrence on time-scales of about 230 ks, though it is not statistically significant ($< 3\sigma$). There is some evidence of phase incoherence, and the dipping episodes sometimes disappear for one or more "cycles". These dips may be produced by accretion instabilities, which would not be periodic.

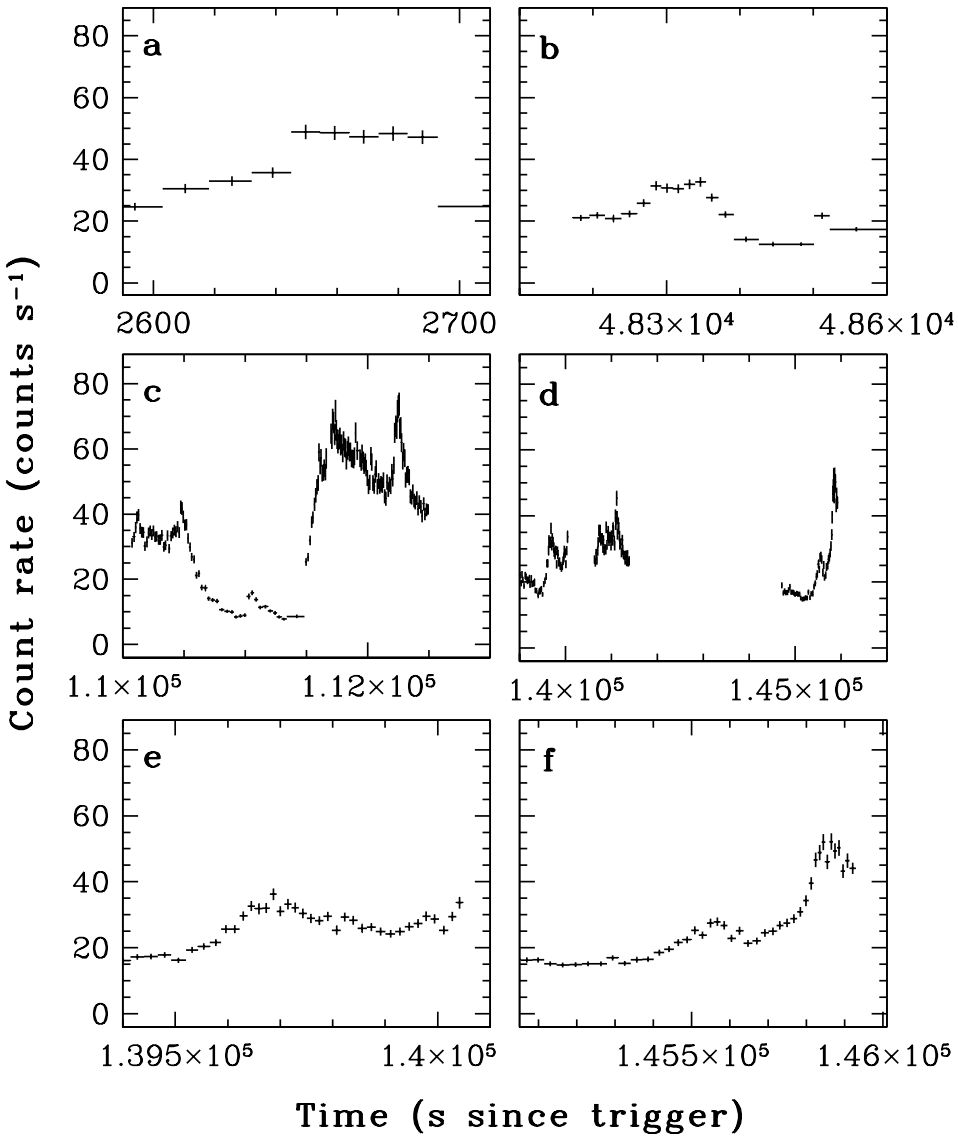

Supplementary Figure 8 | Details of early flares, showing rapid variability. We show the XRT count rate in four time intervals in the early flaring phase of Sw J1644+57 that demonstrate the rapid time variability exhibited by this object. a) Time interval from 2600 – 2700 seconds after the first BAT trigger. Count rate jumps by 37% (4.6σ) in 10.9 s (Supplementary Table 6). b) Time interval: 4.81 – 4.86 ks. Count rate jumps by 74% (7.7σ) in less than 30 s. c) Time interval: 110 – 113 ks. Count rate jumps by 194% (12.7σ), nearly tripling in under 75 s, with two other highly significant increases in count rate in ~ 35 s. d) Time interval: 139 – 147 ks. Several very steeply rising flares. e) Detail of the first flare in interval 4. f) Detail of the last flare in interval 4.

1.5 X-ray Spectral Analysis

Here we discuss the details of our time-resolved spectral analysis of the XRT data, including derivation of time-dependent energy correction factors used to calculate XRT flux light curves.

The XRT data were processed with standard procedures (XRTPIPELINE v0.12.4), filtering and screening criteria by using FTOOLS in the HEASOFT package (v.6.11). We used the latest version of the XRT software task *xrtcalcpi*, which calculates Pulse Invariant (PI) event energies taking into account position dependent corrections for energy losses incurred by charge traps that have developed on the CCD[39]. They are the result of several years of calibration efforts by the XRT team to correct for the effects of radiation damage to the XRT detector after > 6 years in orbit. They provide significant improvements in the spectral resolution and flux calibration compared with earlier versions. We used the latest spectral redistribution matrices:

- WT mode data:
  - swxwt0to2s6_20010101v013.arf
  - swxwt0to2s6_20010101v013.rmf
- PC mode data:
  - swxpc0to12s6_20010101v012.arf
  - swxpc0to12s6_20010101v012.rmf

1.5.1 Simultaneous BAT+XRT Spectral Fits

The BAT and XRT spectra are consistent with each other during the early flares, when the BAT data have enough counts to obtain a useful spectrum. The results of fitting the BAT+XRT spectral data simultaneously for one of the early flares can be seen in Supplementary Figure 9. We find that for this time period the BAT and XRT are fit well by well a broken power-law model. The BAT $15 - 150$ keV spectrum is a continuation of the XRT spectrum, and there is no need for additional spectral breaks or high energy components to fit the BAT spectrum. Unfortunately it is not possible to perform simultaneous fits at all epochs, due to source faintness and the limitations of the Survey data collection mode of the BAT during regular observations. The spectral parameters appear to be strongly dependent on the X-ray flux (see Supplementary Figures 4 – 10). Therefore in order to test whether the BAT spectra were typically consistent with the XRT fits, we fit a broken power-law model to the XRT spectrum at various flux levels, and then extrapolated this model to estimate the expected count rate seen in the BAT energy band. We found that the BAT count rates are highly consistent with the extrapolated XRT spectral fits, suggesting that the consistency seen in the BAT+XRT spectral fit show in Supplementary Figure 9 is true also for later time data.

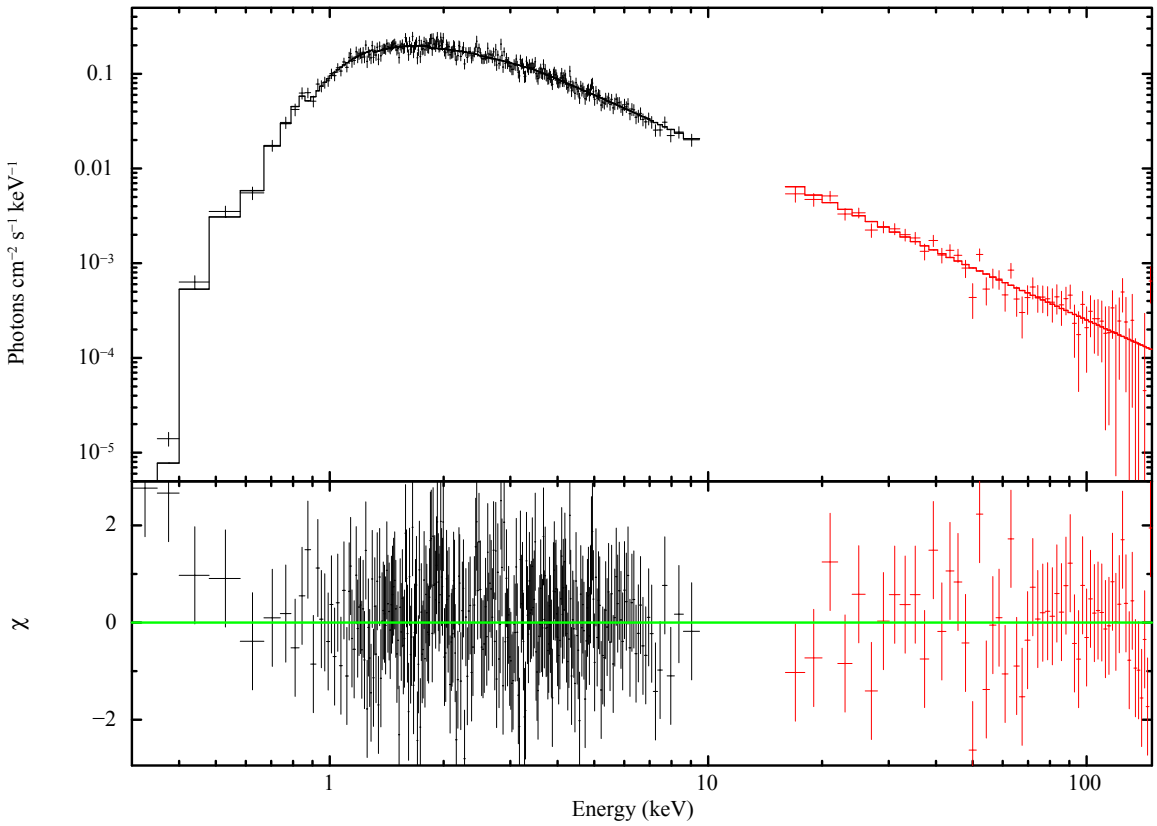

Supplementary Figure 9 | *Swift* combined BAT/XRT "unfolded" spectra for Sw J1644+57. The black points are XRT data and the red points are BAT data. The data are from the time interval 19:57:52.0 – 20:04:32.0 UT on 29 March 2011, during one of the bright flares. This figure shows the spectrum incident on the instruments. The solid line is the fitted broken power-law model. The spectra are equally well-fit by a combination of a multi-temperature disk and a power law.

1.5.2 Intensity-selected XRT Spectra

In order to study variations of X-ray spectral parameters with source brightness, we produced XRT spectra in seven intensity ranges for data collected from March 28 until April 7 2011. Events were accumulated with count rates in the following intervals < 0.5, $0.5-1$, $1-2.5$, $2.5-10$ counts s^{-1} for the PC data, and < 11, $11-35$, > 35 counts s^{-1} for WT data. We corrected the PC data for pile-up by determining the size of an exclusion region at the core of the PSF necessary to get agreement between the wings of the observed PSF and the nominal PSF[37], and excluding from the analysis all the events that fell within that region.

The spectra were fit with several models. In all cases the absorption consisted of two components, one fixed to the Galactic value ($N_{\rm H} = 1.7 \times 10^{20}$ cm^{-2}), and one free at the redshift $z = 0.35$. The following models provided acceptable fits to the data:

1. a simple absorbed power-law model (*tbabs*zwabs(powerlaw)*);
2. a log-parabola model (*tbabs*zwabs(power2)*);
3. a broken power-law model (*tbabs*zwabs(bknpower)*).
4. an absorbed power-law model plus a diskblackbody (*tbabs*zwabs(powerlaw+diskbb)*).

The "power2" log-parabola model is defined as:

$$A(E) = E^{(-\alpha+\beta*\log E)} \tag{1}$$

The spectra are comparably well-fit well by either a log-parabola, a broken power-law or power-law plus multi-temperature thermal model. Fits to simple power laws are generally not quite as good, but statistically acceptable. We observe a strong trend for softer spectra as the source intensity decreases (see Supplementary Figure 10), consistent with the evidence for correlations between the flux and the spectral hardness discussed above. These variations of spectral slope with intensity mean that care must be taken in producing light curves in physical units; the use of single conversion factors (which is commonly done in GRB afterglow light curves, where there is little evidence for spectral varability with time or intensity, outside of bright X-ray flares) will produce inaccurate fluxes.

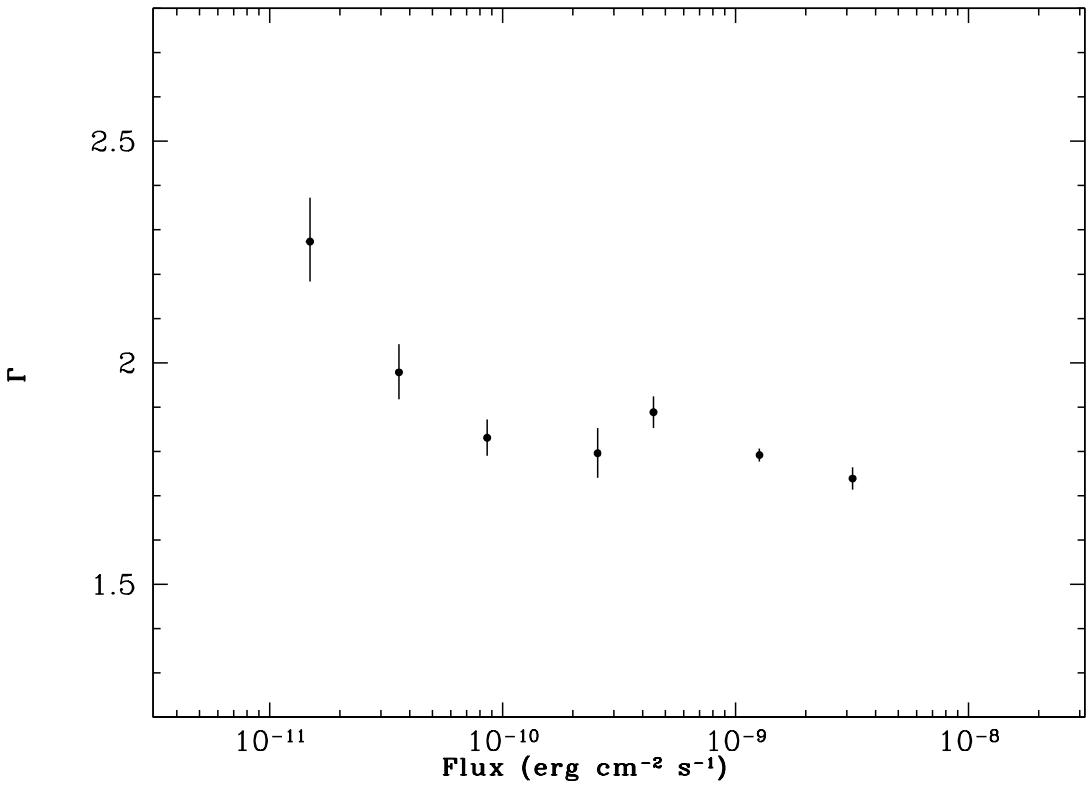

Supplementary Figure 10 | *Swift* XRT intensity-resolved spectral fitting results utilising an absorbed power-law model. Flux is for the 0.3 – 10 keV band. The power law slope is strongly correlated with the count rate, confirming the band ratio results shown in Supplementary Figure 4.

1.5.3 XRT Spectra for SEDs

We extracted spectra for use in our SEDs from three epochs representing three intensity states: *i)* strictly simultaneous with the event-mode BAT spectrum; *ii)* a very low state (4.5 – 5.1 days after the trigger); *iii)* an intermediate state (6.5 – 9.4 days after the trigger). The XRT data for these states are plotted in Supplementary Figures 15 – 17.

1.5.4 Time-selected XRT Spectra

Spectra were also generated from all available XRT data up to 16 May 2011 (observation 50) in order to examine the time dependence of the spectral parameters. We produced spectra with at least 3000 counts, unless strong intensity variations were observed during the integration time interval, in which case shorter integration times were used in order to represent the different intensity states. Hence some spectra were also extracted with fewer counts than 3000. We obtained a total of 42 PC spectra and 163 WT spectra, and we fit them with the first three models described above. The simple power-law model is an adequate description of the data, as is the log-parabola (F-test probabilities $\sim 10^{-3}$). We find that the column density is variable in time with no evidence of increased column when the dips occur. The results of the temporally resolved log-parabola model fits are shown in Supplementary Figure 11; in particular, the harder-when-brighter trend is also observed.

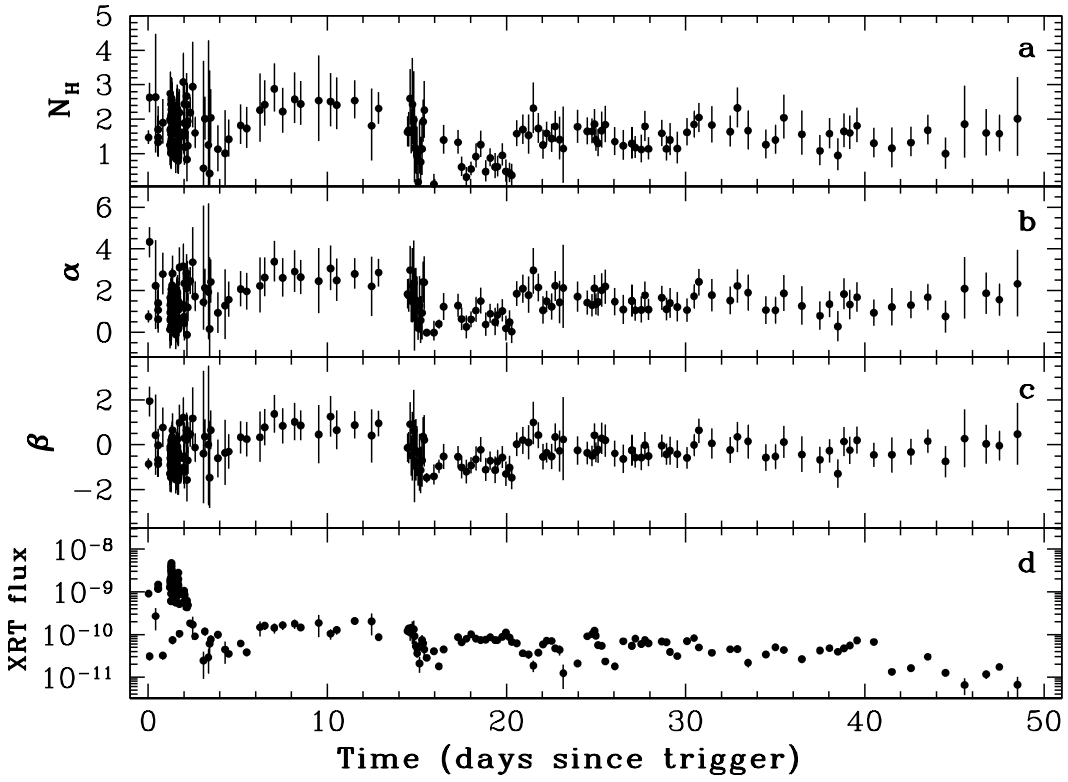

Supplementary Figure 11 | *Swift* XRT time-resolved spectral fitting utilising an absorbed log-parabola model. Parameters α and β for the log-parabola model are as defined in Supplementary Equation 1. $N_{\rm H}$ is the redshift corrected intrinsic absorption in units of 10^{22} cm^{-2}, XRT flux is the observed flux in units of erg cm^{-2} s^{-1}(0.3−10 keV).

1.6 Flux-calibrated X-ray Light Curves

The results of the time-resolved spectral analysis with the log-parabola fits (Supplementary Figure 11) were used to calculate energy conversion factors (ECFs; see Supplementary Figure 12) for conversion from the XRT count rate light curve shown in Supplementary Figure 2 to the flux-calibrated light curves presented in Figure 2 of the main Letter and in Supplementary Figure 13 below. We used absorption-corrected fluxes in the 1 – 10 keV band to calculate ECFs for each time-resolved spectrum. We then interpolated these ECFs to the time of each bin in the count rate light curve of Supplementary Figure 2. The interpolated ECFs were multiplied by the counts in each light curve bin to obtain the absorption-corrected flux light curve.

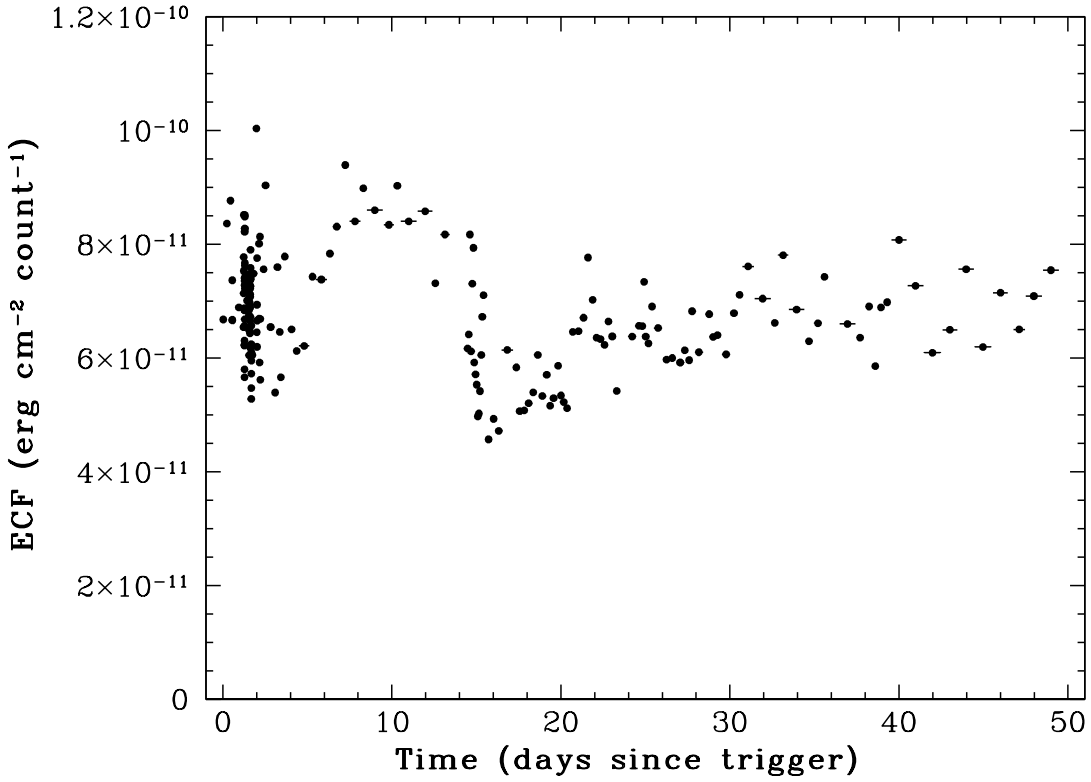

Supplementary Figure 12 | Time-Dependent 1-10 keV Energy Conversion Factors. Energy conversion factors (ECFs) derived from time-dependent spectral fits to the *Swift* XRT data for Sw J1644+57. These factors were used to convert the light curve in counts per second to a light curve in flux units.

We used the 1 – 10 keV band for our flux light curves to reduce systematic uncertainties arising from the large absorption corrections needed to calculate source flux in the observed 0.3 – 1 keV band. There is still some systematic uncertainty in the ECFs caused by uncertainties in the fitting parameters of the spectral fits. The variations in ECF in the 25-50 day range can be taken as an indication of the residual systematic uncertainties in the fluxes, which amount to $\sim \pm 15\%$. These have not been included in the flux light curves presented here, which show only uncertainties due to counting statistics. (We note that these systematics also introduce a $\pm 15\%$ scatter in the flux light curves, but this is small compared to the strong variability in the count rates.)

The flux light curve was used to estimate the total X-ray energy output of Sw J1644+57. The total measured unabsorbed fluence in the 1 – 10 keV band is 7.3×10^{-5} erg cm^{-2}. Correcting for the duty cycle of the observations, this gives a total unabsorbed fluence for Sw J1644+57 of 5.1×10^{-4} erg cm^{-2} in the observed 1 – 10 keV band for the first

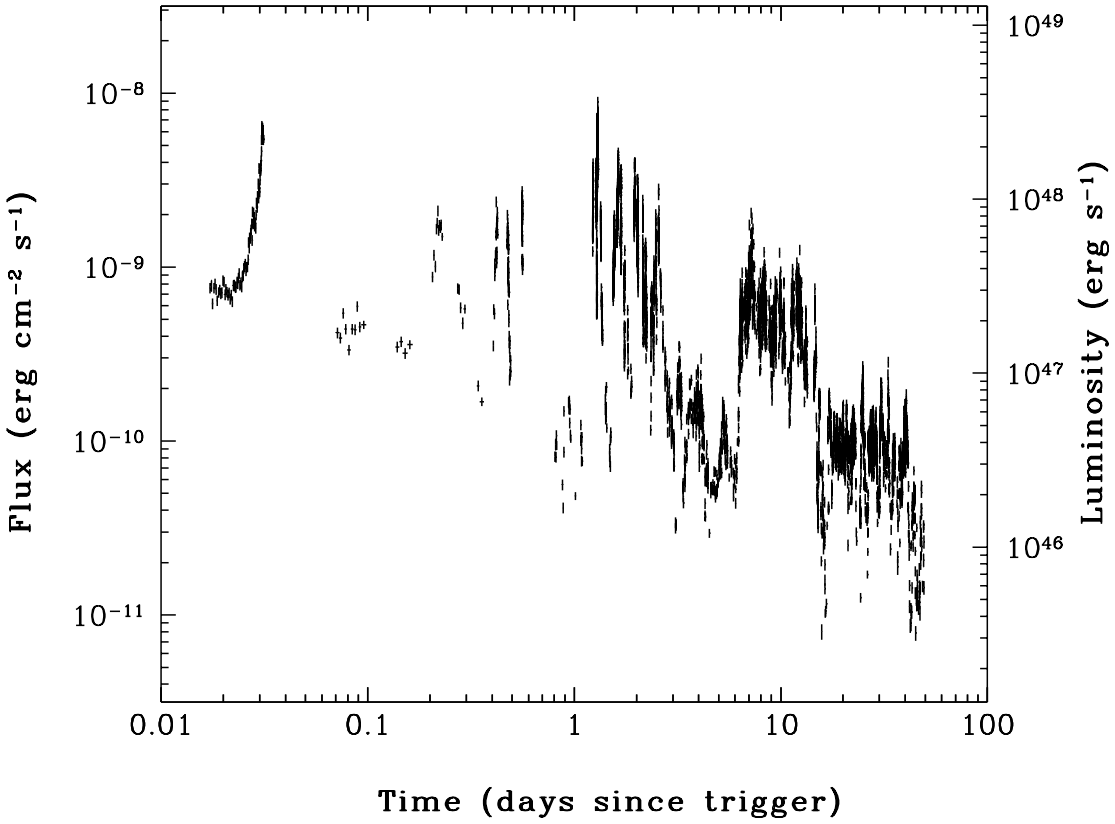

Supplementary Figure 13 | *Swift* XRT flux light curve of Sw J1644+57, through 17 May 2011. .

50 days after the first BAT trigger. Each flux point in the light curve was also converted to a luminosity at the source, and these were summed to obtain an estimate of the total X-ray energy (corrected for live-time fraction) of 2×10^{53} erg in the 1.35 – 13.5 keV rest frame energy band. Mean, median, peak and minimum flux and luminosity values for Sw J1644+57 are given in Supplementary Table 7. For the SEDs discussed in SI§2.3, the X-ray band accounts for between $\sim 20\%$ (during the bright flares) and $\sim 60\%$ (during the low state) of the bolometric luminosity (see Supplementary Table 13). The total radiative energy output is therefore several times the values given in Supplementary Table 7.

Supplementary Table 7 | X-ray Rest Frame Flux and Luminosity of Sw J1644+57.

	Observer frame	Rest frame
Flux Level	Unabsorbed Flux (1.0 – 10.0 keV)	Luminosity (1.35 – 13.5 keV)
Maximum	6.9×10^{-9} erg cm^{-2} s^{-1}	2.9×10^{48} erg s^{-1}
Mean	6.5×10^{-10} erg cm^{-2} s^{-1}	2.7×10^{47} erg s^{-1}
Median	2.0×10^{-10} erg cm^{-2} s^{-1}	8.5×10^{46} erg s^{-1}
Minimum	6.8×10^{-12} erg cm^{-2} s^{-1}	2.8×10^{45} erg s^{-1}

1.7 Historical X-ray/γ-ray Upper Limits

Here we demonstrate that this object was in a much lower flux state during previous serendipitous observations.

We have examined archival databases from several X-ray and γ-ray instruments that have observed the location of Sw J1644+57, either through wide field surveying or in serendipitous pointings, to search for earlier detections of a source from this direction at a variety of wavelengths. In all cases, we have calculated flux upper limits in the 1 – 10 keV band for direct comparison to the XRT flux light curves for Sw J1644+57. This band was chosen to minimize systematic uncertainties caused by the correction for absorption at energies below 1 keV. Several spectral models that provide good fits to the *Swift* XRT data were used for the extrapolations; the variation in upper limits gives some feeling for systematic uncertainties associated with both the N_H correction and the energy extrapolation. In all cases, the least restrictive upper limits were plotted in Figure 2 of the Letter.

1.7.1 *ROSAT* Historical Upper Limits

Sw J1644+57 was serendipitously observed in a 6.5 ks *ROSAT* PSPC-B observation made on 3 April 1992 covering the energy range $0.1-2.35$ keV. The source is $\sim 42'$ off axis and is affected by shadowing from one of the PSPC windows support ribs, giving an effective exposure time of 3.3 ks. The 3σ upper limit[56] for the PSPC count rate is 8.3×10^{-3} counts s^{-1}, corresponding to an observed $1-10$ keV flux limit of $<2.8\times10^{-13}$ erg cm^{-2} s^{-1} for any of the spectral models that fit the XRT data. We note that no source is detected at even the 1.5σ level. This limit is more than an order of magnitude below the faintest portion of the XRT light curve, and nearly four orders of magnitude below the brightest flares. Upper limits on the flux for different spectral models for Sw J1644+57 are given in Supplementary Table 8.

The *ROSAT* All-Sky Survey also covered this field with a relatively long exposure due to its high ecliptic latitude, collecting 940 s of data between 11 July 1990 and 13 August 1991. These data provide a 3σ PSPC count rate upper limit[56] of 7.3×10^{-3} counts s^{-1}, with a corresponding 1 – 10 keV flux limit of $<2.5\times10^{-13}$ ergs cm^{-2} s^{-1}.

Supplementary Table 8 | *ROSAT* 3σ upper limits (1 – 10 keV) for Sw J1644+57 for 3 spectral models

	RASS Observation		3 April 1992 Pointed Observation	
Model	Observed Flux†	Unabsorbed Flux†	Observed Flux†	Unabsorbed Flux†
Simple absorbed power law model ($N_{\rm H}=7.7\times10^{21}$ cm^{-2}, $\Gamma=2.8$):				
	$<2.41\times10^{-13}$	$<3.63\times10^{-13}$	$<2.76\times10^{-13}$	$<4.16\times10^{-13}$
Broken power law model ($N_{\rm H}=1.30\times10^{22}$ cm^{-2}, $\Gamma_1=4.98$, $E_{break}=1.96$ keV, $\Gamma_2=2.48$):				
	$<2.43\times10^{-13}$	$<5.75\times10^{-13}$	$<2.78\times10^{-13}$	$<6.59\times10^{-13}$
Disk black body + power law model ($N_{\rm H}=1.24\times10^{22}$ cm^{-2}, $T_{\rm in}=175$ eV, $\Gamma=2.4$, $R^{\ddagger}=2.2\times10^{6}$):				
	$<2.44\times10^{-13}$	$<5.48\times10^{-13}$	$<2.80\times10^{-13}$	$<6.28\times10^{-13}$

†All fluxes are 3σ upper limits in erg cm^{-2} s^{-1} (1.0 – 10.0 keV in the observed frame).
$^{\ddagger}R$ = ratio of flux normalizations between the *diskbb* and *plaw* models.

1.7.2 *XMM-Newton* Historical Upper Limits

Although there were no pointed observations of the Sw J1644+57 field by *XMM-Newton* prior to the outburst, between 26 August 2001 and 25 March 2011 *XMM-Newton* slewed over this object on one occasion at 01:42:32 UT on 27 July 2005. The EPIC-pn instrument routinely takes data during such slews[57], with results reported on the ESA *XMM-Newton* website (*http://xmm.esac.esa.int/external/xmm_products/slew_survey/upper_limit/uls.shtml*). Sw J1644+57 was not detected during the 3.9 s exposure made with the medium filter, resulting in a 3σ upper limit of < 1.5 counts s^{-1} (0.2 – 12 keV), calculated following the Bayesian approach of Kraft, Burrows & Nousek[56]. Observed and unabsorbed 1 – 10 keV flux limits were derived for the three spectral models described in Supplementary Table 8 and are given in Supplementary Table 9.

Supplementary Table 9 | *XMM-Newton* Slew Survey 3σ upper limits (1 – 10 keV) for Sw J1644+57 for 3 spectral models

	XMM-Newton Observation on 27 July 2005	
Model	Observed Flux†	Unabsorbed Flux†
Simple absorbed power law model ($N_{\rm H} = 7.7 \times 10^{21}$ cm^{-2}, $\Gamma = 2.8$):		
	$< 5.1 \times 10^{-12}$	$< 7.6 \times 10^{-12}$
Broken power law model ($N_{\rm H} = 1.30 \times 10^{22}$ cm^{-2}, $\Gamma_1 = 4.98$, $E_{break} = 1.96$ keV, $\Gamma_2 = 2.48$):		
	$< 5.5 \times 10^{-12}$	$< 1.3 \times 10^{-11}$
Disk black body + power law model ($N_{\rm H} = 1.24 \times 10^{22}$ cm^{-2}, $T_{\rm in} = 175$ eV, $\Gamma = 2.4$, $R^{\ddagger} = 2.2 \times 10^{6}$):		
	$< 5.5 \times 10^{-12}$	$< 1.2 \times 10^{-11}$

†All fluxes are 3σ upper limits in erg cm^{-2} s^{-1} (1.0 – 10.0 keV in the observed frame).
‡R = ratio of flux normalizations between the *diskbb* and *plaw* models.

1.7.3 *MAXI* Historical Upper Limits

To investigate whether *MAXI* detected the Sw J1644+57 before the current outburst, we have analysed historical *MAXI* GSC data for the period of 17 August 2009 to 1 March 2011 (see Supplementary Figure 14). No detection of Sw J1644+57 is found in those data, giving a 90% confidence level upper limit of $\sim 1.1 \times 10^{-11}$ erg cm^{-2} s^{-1} (2 – 20 keV). In addition to this, utilising data that has had additional cleaning applied, but covers a narrower time period (between 1 September 2009 and 31 March 2010), we obtain a deeper 90% confidence level upper limit of 2.7×10^{-12} erg cm^{-2} s^{-1} (4 – 10 keV). The corresponding 3σ upper limits for the 1 – 10 keV band are given in Supplementary Table 10.

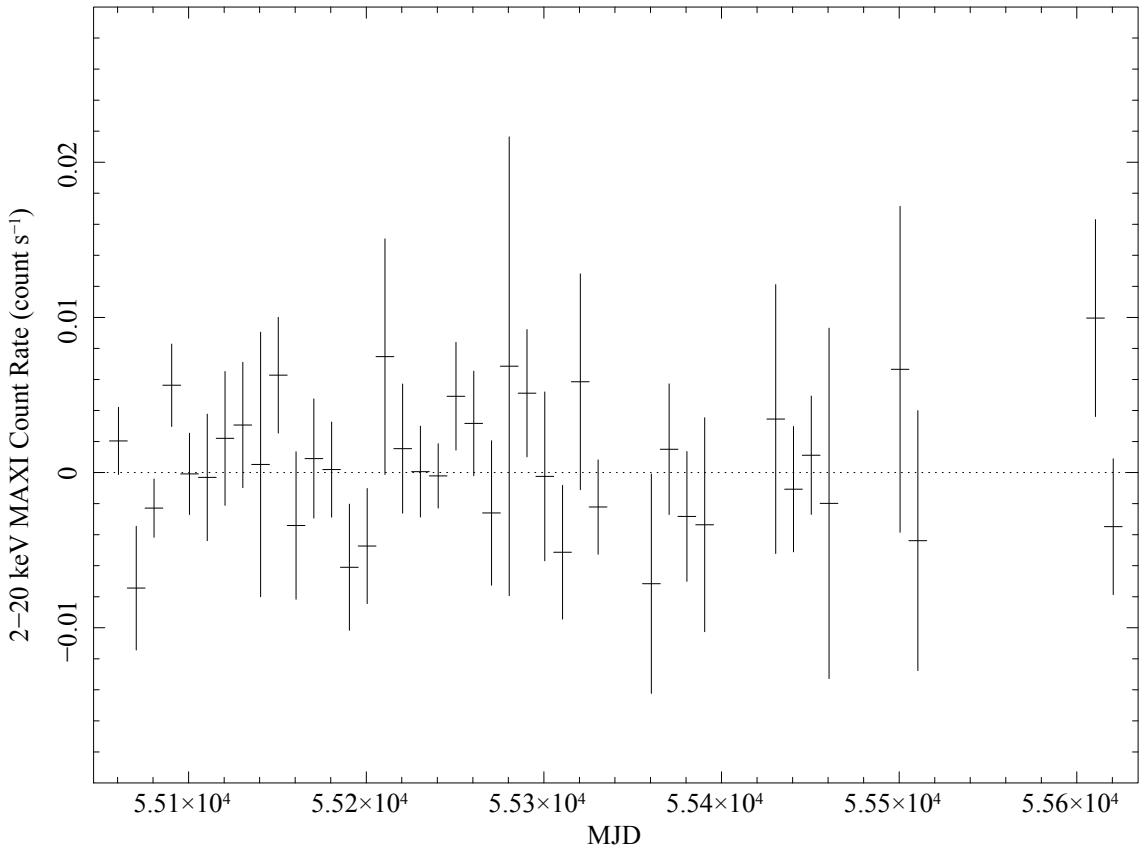

Supplementary Figure 14 | *MAXI* light curve of Sw J1644+57 for the period August 17 2009 to 1 March 2011. Note that the count rates seen in this light curve are consistent with a non-detection of Sw J1644+57 in this period.

Supplementary Table 10 | *MAXI* 3σ upper limits (1 – 10 keV) for Sw J1644+57 for 3 spectral models

	1 September 2009 – 31 March 2010	
Model	Observed Flux[†]	Unabsorbed Flux[†]
Simple absorbed power law model ($N_{\rm H} = 7.7 \times 10^{21}$ cm^{-2}, $\Gamma = 2.8$):		
	$< 1.7 \times 10^{-11}$	$< 2.6 \times 10^{-11}$
Broken power law model ($N_{\rm H} = 1.30 \times 10^{22}$ cm^{-2}, $\Gamma_1 = 4.98$, $E_{break} = 1.96$ keV, $\Gamma_2 = 2.48$):		
	$< 1.4 \times 10^{-11}$	$< 3.4 \times 10^{-11}$
Disk black body + power law model ($N_{\rm H} = 1.24 \times 10^{22}$ cm^{-2}, $T_{\rm in} = 175$ eV, $\Gamma = 2.4$, $R^{\ddagger} = 2.2 \times 10^{6}$):		
	$< 1.4 \times 10^{-11}$	$< 3.2 \times 10^{-11}$

[†]All fluxes are 3σ upper limits in erg cm^{-2} s^{-1}(1.0 – 10.0 keV in the observed frame).
[‡]R = ratio of flux normalizations between the *diskbb* and *plaw* models.

1.7.4 BAT Historical upper limits

The BAT instrument monitors about 80% of the sky daily, and the BAT data are searched daily in the 15-50 keV band for transient events. We examined the entire BAT data set from 12 February 2005 to 28 March 2011, searching for previous detections of Sw J1644+57 on three timescales. The source is not detected on 16-day timescales, with a 3σ upper limit of 0.0011 counts cm^{-2} s^{-1}(about 5 mCrab, 15-50 keV). On 1-day timescales, we obtain marginal detections exceeding 3σ on 31 March 2009, 14 September 2009, and 14 March 2011, all at about 0.0036 ± 0.0011 counts cm^{-2} s^{-1} (15-50 keV); this detection rate is consistent with the expected rate of false 3σ fluctuations in a search of 1866 independent measurements, and we therefore do not consider these detections to be significant. With the exception of these three days, the 1-day 3σ upper limits vary depending on the total exposure of the source, but are between 0.0010 and 0.0015 counts cm^{-2} s^{-1} (15-50 keV) for 90% of the observations. On shorter timescales, we can state that the source never exceeded the 6σ significance level on any timescale between 64 s and 1200 s when it was in the BAT field of view (count rate and flux limits vary with each observation) until it triggered the BAT in a 1200 second image trigger on 28 March 2011.

The BAT survey data have been integrated over long time intervals to produce the most sensitive surveys of the sky ever made in the 15 – 150 keV band[58]. These surveys can be used to place sensitive limits on steady-state emission from Sw J1644+57 in the BAT energy range since December 2004. Sw J1644+57 was not found in any of the BAT survey studies[59,60,58] down to a limiting flux of $\sim 10^{-11}$ erg cm^{-2} s^{-1} (15-150 keV), about two orders of magnitude below the average flux measured by BAT in the first 3 days after the BAT trigger, and three orders of magnitude lower than the peak fluxes measured by BAT during the brightest flares. The strongest long-term upper limit is from the 70 month BAT Survey[58], which provides a 3σ flux limit in the 14-195 keV band of 5.4×10^{-12} erg cm^{-2} s^{-1}; this value should be used to compare to the BAT fluxes measured since the trigger. In Supplementary Table 11 we provide 1 – 10 keV upper limits based on the 70 month BAT Survey for direct comparison to the XRT observations of Sw J1644+57. These upper limits are shown in Figure 2 of the Letter.

Supplementary Table 11 | BAT 70 Month Survey[58] 3σ upper limits (1 – 10 keV) for Sw J1644+57 for 3 spectral models

Model	Unabsorbed Flux†
Simple absorbed power law model ($N_{\rm H} = 7.7 \times 10^{21}$ cm^{-2}, $\Gamma = 2.8$):	$< 4.3 \times 10^{-11}$
Broken power law model ($N_{\rm H} = 1.30 \times 10^{22}$ cm^{-2}, $\Gamma_1 = 4.98$, $E_{break} = 1.96$ keV, $\Gamma_2 = 2.48$):	$< 3.1 \times 10^{-11}$
Disk black body + power law model ($N_{\rm H} = 1.24 \times 10^{22}$ cm^{-2}, $T_{\rm in} = 175$ eV, $\Gamma = 2.4$, $N^{\ddagger}_{disk} = 1.84 \times 10^{4}$):	$< 3.0 \times 10^{-11}$

†All fluxes are 3σ upper limits in erg cm^{-2} s^{-1}(1.0 – 10.0 keV in the observed frame).
$^{\ddagger}N_{disk}$ = flux normalization for the *diskbb* model (fixed to the value found for the XRT fit to this model).

1.7.5 *Fermi* Historical Upper Limits

The analysis of the full 32-month *Fermi*/LAT dataset does not reveal any new source within 3 degrees of the position of the transient. This places 95% confidence upper limits of 1.7×10^{-8} photons cm^{-2} s^{-1} (100 MeV-10 GeV) and 1.5×10^{-10} photons cm^{-2} s^{-1} (1 GeV - 300 GeV) on any persistent prior emission. Given the variable nature of this source, a search for emission was performed on shorter timescales of 2 days and 5 days over the *Fermi* mission lifetime. No significant variation from the mean background level is observed.

2 Discussion

Here we provide additional details on the theoretical interpretation of our results, expanding on the points raised in the main body of our Letter.

2.1 Constraints on the Mass of the Central Black Hole

This section provides additional details on our estimates of the mass of the accreting black hole.

An upper limit to the mass of the central black hole in the galaxy where the transient was observed can be obtained through the black hole mass *vs* host bulge luminosity relation[61]. Using the measured B and H magnitudes of the host galaxy from published reports[62,63] and from our own analysis of *Hubble Space Telescope* WFC3 observations, and taking a luminosity distance of $d_{\rm L} = 1.88$ Gpc, we infer the following luminosities relative to the Sun: $\log(L_{\rm B}/L_{\odot,{\rm B}}) = 9.20$ and $\log(L_{\rm H}/L_{\odot,{\rm H}}) = 9.58$ (the B-band luminosity includes a Galactic extinction correction of $A_{\rm B} = 0.08$ mag). These luminosity estimates lead to a black hole mass of $M_{\rm bh} \approx 2 \times 10^7$ M$_\odot$, with a systematic uncertainty of a factor of 2–3 resulting from the scatter in the empirical relation between the host luminosity and black hole mass[64]. This empirical formula relates the luminosity of the *spheroid* of the host galaxy (i.e, its bulge) to the black hole mass. In the HST optical image the host galaxy is barely resolved and we cannot characterize the galaxy morphology. The spectrum of the host galaxy shows the spectroscopic signature of star formation[65], but the B-R color of the host galaxy is 1.5, which is in the range occupied by E and S0 galaxies (from 1.39 to 1.57)[66]. This leads us to conclude that the bulge mass is a substantial fraction of the total mass of the host. However, since the magnitudes we have used refer to the entire galaxy, not just its bulge, the above value is an upper limit to the black hole mass. On the other hand, if there is substantial evolution in the black-hole/bulge scaling relations at this redshift[67], the mass could be somewhat higher than our estimate suggests. In any event, the properties of the host galaxy place the central black hole mass near the low end of the $10^7 - 10^9$M$_\odot$ range typical of AGNs.

An independent constraint on the black hole mass can be obtained from the minimum X-ray variability time scale, which is observed to be $\Delta t_{\rm min} \sim 100$ s (3σ value). This variability time scale constrains the size of the black hole under the assumption that the central engine dominates the variability. (More rapid TeV variability has been observed in some blazars, which may be attributed to additional local Lorentz boost within a jet (e.g. jet in the jet)[68].) For a Schwarzschild black hole, the minimum variability time scale in its rest frame is $\Delta t_{\rm min} \sim r_{\rm S}/c \sim 100\, M_6$ s, where $M_6 = M_{\rm bh}/10^6 M_\odot$. Thus,

$$M_{\rm bh} \sim 7.4 \times 10^6 \left(\frac{\Delta t_{\rm obs}}{100\ {\rm s}}\right) M_\odot\ . \qquad (2)$$

Much larger or much smaller masses are unlikely for the following reasons. For larger masses, a variability time scale much shorter than the above constraint has not been observed in the X-ray band in other systems containing supermassive black holes (e.g. AGNs). For much smaller masses (e.g. stellar-mass black holes), one would expect to see much shorter variability time scales in the light curves.

This estimate is really an upper limit, since variability on the timescale allowed by the size of the black hole is not assured. In fact, some nearby low-luminosity GRBs with a stellar-mass central engine (e.g. GRB 060218) have a smooth light curve without a noticeable fast variability component. However, GRB 060218 has only one peak. It would be contrived to have a smaller black hole smear up all the shorter variability time scales but only keep the > 100 s time scale. We conclude that the black hole mass is likely $M_{\rm bh} \sim (10^6 - 2 \times 10^7) M_\odot$ ($1 < M_6 < 20$).

2.2 Energetics and Mass Accretion Rate

Based on the X-ray light curve, we can make some estimates of the total luminosity (power) of the source, its total energy production, and the inferred mass accretion rate.

After the initial flare, the X-ray flux of Sw J1644+57 was $F_{\rm X} \sim 10^{-10}$ erg cm^{-2} s^{-1} for many weeks. The X-ray luminosity is

$$L_{\rm X,iso} = 4.2 \times 10^{46}\ {\rm erg\ s^{-1}} \left(\frac{F_{\rm X}}{10^{-10}\ {\rm erg\ cm^{-2}\ s^{-1}}}\right), \qquad (3)$$

assuming the above luminosity distance and isotropic emission. This luminosity is well above the Eddington limit for a 10^6 $M_\odot$ black hole ($L_{\rm Edd} = 1.3 \times 10^{44} M_6$ erg s^{-1} with $M_{\rm bh} = 10^6 M_6$ $M_\odot$), suggesting that the emission originates from a relativistic jet rather than an accretion disk.

The above luminosity, along with the coincidence of the event with the centre of the host galaxy[63], led us to consider the onset of accretion-powered nuclear activity in the host galaxy. This could be fueled either by the tidal disruption of a star by the central black hole[69] or by the supply of gas from another source.

The mass accretion rate can be estimated as $\eta \dot{M} c^2 = L/f$, where η is the radiation efficiency, while f is the beaming factor. This gives

$$\dot{M} = 2.3 \times 10^{-8}\ {\rm M}_\odot\ {\rm s}^{-1} \left(\frac{F_{\rm X}}{10^{-10}\ {\rm erg\ cm^{-2}\ s^{-1}}} \right) (f\eta)^{-1}\ . \quad (4)$$

The total accreted mass is related to the total fluence $\mathscr{F}$ by

$$M = 0.023\ {\rm M}_\odot \left(\frac{\mathscr{F}_{\rm X}}{10^{-4}\ {\rm erg\ cm^{-2}}} \right) (f\eta)^{-1}\ . \quad (5)$$

Typically, we expect $\eta \leq 1$ and $f \geq 1$, so that $f\eta \sim 1$.

As of 16 May 2011, the total 1-10 keV X-ray fluence recorded by Swift was 5×10^{-4} erg cm^{-2} (SI§1.6). The bolometric fluence is several times that (for our favored broad-band spectral model, the X-ray flux varies from 50% of the total during the bright flares to $\sim 20\%$ of the total bolometric flux during the low flux states). This gives a total accreted mass at least $(0.2/(f\eta))\,{\rm M}_\odot$. We note that models of tidal disruption events suggest that up to 50% of the mass of the disrupted star might be captured by the black hole; the inferred accreted mass for Sw J1644+57 is consistent with these predictions.

2.3 Modeling the Spectral Energy Distribution of the Emerging Jet

We now address the details of our model of the Spectral Energy Distribution of Sw J1644+57. In this subsection we summarize the data used for this effort, discuss assumptions of our modeling approach and observational constraints imposed on the model parameters, and briefly discuss the modeling procedure. In the following subsections we discuss the input parameters we adopted for the SED models, followed by a detailed discussion of three different SED models. We then briefly discuss an interpretation based on a magnetically-dominated jet in the context of a GRB model (SI§2.8), and show that this model comes to the same basic conclusions as our preferred blazar model.

2.3.1 Available Data

Here we summarize the data available to us for SED modeling:

Radio Observations – The 8.4 GHz flux density was observed on 1 April[70]. The 13.5 GHz, 15 GHz and 100 GHz (3 mm) fluxes were also reported in GCN Circulars[71,72,73]. Although important, these data will not be used to for the modeling of the X-ray and IR emitting region, since the radio emission must come from a larger region, not to be self-absorbed. Additional radio observations and their interpretation are treated by Zauderer et al.[74].

IR and Optical Observations – In SI§1.2 we present our optical and near-infrared observations. Of these data, we have selected for the modeling those corresponding to the peak of the X-ray/γ-ray light curve (approximately 2 days after trigger), at the first minimum of the X-ray light curve ($\sim$4.5 days), and at an intermediate state about a week after the trigger. The large column density derived from the X-ray fitting, of the order of $N_{\rm H} \sim 10^{22}$ cm^{-2}, suggests a large value of the extinction, even if the dust to gas ratio is not known. We de-redden our data with a rest frame $A_V = 4.5$, as discussed in the SI§1.2.

X-Ray Observations – We have chosen to show the spectra for the peak (31 hours from trigger), including BAT data; for the minimum after 4.5 days; and for the intermediate persistent flux state that began a few days after the first BAT trigger.

γ-ray Observations – We use the upper limit in the *Fermi*/LAT band reported in the SI§1.3.2.

TeV Observations – The *VERITAS* Collaboration set upper limits on VHE emission during the early "flaring" period 29 – 31 March and the later "quiescent" period, 1 – 15 April[75]. The two upper limits are reported in the SED shown in Supplementary Figure 15 – 17.

2.3.2 Assumptions and Observational Constraints on the Model

We assume that the spectrum is produced by the synchrotron and inverse Compton (IC) mechanisms. In general, the seed photons for the inverse Compton process can be produced by the synchrotron process itself (Synchrotron Self-Compton, SSC) or can be produced outside the jet (External Compton, EC). A new-born blazar (if that is what Sw J1644+57 is) has had no time to build up a broad line region (i.e., to populate the surroundings of the jet with external photons), but some contribution to the EC process can come from photons produced in the accretion disk. The following is a summary of information we have used to guide the development of the model:

- The variability timescale, $\Delta t_{\rm v} = \Delta t_{\rm obs} \sim 100$ s, places a limit on the size of the X-ray emitting region.
- The isotropic luminosity $L_{\rm obs}$ at the peak of the flare is $L_{\rm obs} = 10^{48} L_{\rm syn,48}$ erg s^{-1}; there is variability by a factor > 100.
- We have some hints on the peak energy, since *Fermi*/LAT and *VERITAS* did not detect the source.
- The slope of the line connecting the NIR to the X-rays is hard, possibly as hard as $\nu^{1/3}$ (the exact slope depends on the amount of extinction assumed).
- This is the first time we have ever observed a flare of this kind, therefore the phenomenon is relatively rare.
- The upper limit on the black hole mass derived above is 2×10^7 M$_\odot$, and a mass compatible with the observed variability is $\sim 7 \times 10^6$ M$_\odot$.

For blazar jets, one can find a unique solution for modeling their spectral energy distribution (SED) when the emission is SSC, and when we know the peak frequencies of the synchrotron and Compton spectra, the slopes before and after the peaks, the peak flux levels, and the variability timescale. Here we do not know anything about the Compton component, and we can only guess the peak frequency (and flux) of the synchrotron component. Therefore we need additional assumptions in order to find a reasonable fit.

One possibility is to assume that: (*i*) the source is magnetically dominated (note that this is *not* the case for blazars, whose jet powers are dominated by the kinetic energy of particles), and (*ii*) the self Compton flux must be absorbed by the γ–$\gamma \rightarrow e^{\pm}$ process. The first assumption comes from the very hard optical to X-ray spectrum, requiring a low energy cut-off in the particle distribution, and thus indicates a particle-starved jet, whilst the second requirement comes from the *Fermi* and *VERITAS* upper limits.

An alternative would be to tie the NIR and radio data together as a single syncrotron component, with the X-rays as inverse Compton[74,76]. This interpretation requires that the extinction be much lower than $A_V = 4.5$, so that the extinction correction is small and the slope of the optical/NIR SED at the source is negative. This does not agree with our best-fit determination of the extinction and seems in conflict with the X-ray absorption column density. It also requires that the NIR-to-X-ray slope coincidentally mimics a synchrotron spectrum. We think this is an unlikely coincidence, but we discuss it further below.

The size – We assume for simplicity a spherical source of radius R at some distance d from the black hole. We define $\mathscr{D} \equiv 1/[\Gamma(1-\beta\cos\psi_{\rm v})]$ as the Doppler factor, where $\psi_{\rm v}$ is the viewing angle. Note that for blazars one assumes a mono-directional velocity (unlike in GRBs). The size is constrained by:

$$R \leq c\Delta t_{\rm obs}\frac{\mathscr{D}}{1+z} \qquad (6)$$

Magnetic field – We assume that the bulk of the luminosity is produced by synchrotron radiation. We further assume that the jet is magnetically dominated. This is because of the very hard slope between the optical and the X-rays, implying that there are no low energy electrons in the source. If there were, then they would severely overproduce the optical flux. One possibility is that the electrons are continuously reaccelerated/heated, in such a way that there are no electrons below, say, $\gamma \sim 10^2 - 10^3$. So we need a "thermal bath", but with relatively few electrons inside. Otherwise the mean energy of the particles will be small. As a consequence, the jet is particle-starved, and the jet power must be carried by the magnetic field. The jet is however capable of producing a lot of radiation: the isotropic luminosity we see is $L_{\rm obs} \sim 10^{48}$ erg s^{-1}, but this is beamed. The real power spent by the jet to produce $L_{\rm obs}$ is

$$P_{\rm r} \sim \frac{L_{\rm obs}}{\Gamma^2} \tag{7}$$

up to a factor of order unity[77]. If the jet is particle-starved, this power must be given by the Poynting flux, and therefore we require:

$$P_{\rm B} = \pi R^2 \Gamma^2 c \frac{B^2}{8\pi} > \frac{L_{\rm obs}}{\Gamma^2} \tag{8}$$

Together with Supplementary Equation 6 this gives the limit:

$$B > \frac{1+z}{\Gamma^2 \mathscr{D} \Delta t_{\rm obs}} \left(\frac{L_{\rm obs}}{8c^3} \right)^{1/2} \tag{9}$$

Pair production – Since we are dealing with a compact source, with a large produced synchrotron luminosity, it is conceivable that the self-Compton emission would be relevant. But the upper limits by *Fermi* tell us that the observed γ-ray flux is much less than the synchrotron flux. One way to account for that is pair opacity. We may therefore require that the optical depth for pair production is larger than unity:

$$\tau_{\gamma\gamma} \sim \frac{\sigma_{\rm T}}{5} \frac{U'_{\rm ssc}}{m_{\rm e}c^2} R > 1 \tag{10}$$

where $U'_{\rm ssc}$ is the comoving synchrotron self-Compton radiation energy density, and $U'_{\rm ssc}/m_{\rm e}c^2$ is (very approximately!) the number density of photons at threshold, where $\sigma_{\gamma\gamma} \sim \sigma_{\rm T}/5$. We then have:

$$\frac{\sigma_{\rm T}}{5} \frac{L'_{\rm ssc}}{4\pi R^2 c m_{\rm e} c^2} R = \frac{\sigma_{\rm T}}{20\pi} \frac{L'_{\rm ssc}}{L'_{\rm syn}} \frac{(L_{\rm syn}/\mathscr{D}^4)}{R m_{\rm e} c^3} = \frac{\sigma_{\rm T}}{20\pi} \frac{L'_{\rm ssc}}{L'_{\rm syn}} \frac{L_{\rm syn}(1+z)}{\mathscr{D}^5 c \Delta t_{\rm obs} m_{\rm e} c^3} > 1 \tag{11}$$

Distance from the black hole – If we assume a conical jet of semi-aperture angle $\theta \equiv 0.1\theta_{-1}$ we have

$$d \sim \frac{R}{\theta} < \frac{10 c \Delta t_{\rm obs} \mathscr{D}}{\theta_{-1}(1+z)} \tag{12}$$

Since we continue not to detect the source in γ-rays, whilst the X-rays vary widely, it is likely that we are observing some sort of a standing shock, or (magnetically dominated) internal shocks. The emission cannot be due to a single traveling blob. A single blob would travel rapidly, expand, and die in a short time.

Some numbers – From Supplementary Equation 11 we can set a limit on the Doppler factor, $\mathscr{D}$:

$$\mathscr{D} < 11.4 \left(\frac{L_{\rm syn,48}}{\Delta t_{\rm obs,2}} \frac{L'_{\rm ssc}}{L'_{\rm syn}} \right)^{1/5} \tag{13}$$

where $\Delta t_{\rm obs} \equiv 10^2 \Delta t_{\rm obs,2}$ s. Using this limit in Supplementary Equation 9, we derive a lower limit on B:

$$B > 620 \frac{(\mathscr{D}/\Gamma)^3}{L_{\rm syn,48}^{1/10} \Delta t_{\rm obs,2}^{2/5}} \left(\frac{L'_{\rm syn}}{L'_{\rm ssc}} \right)^{3/5} \text{ Gauss} \tag{14}$$

The size should be:

$$R < 2.5 \times 10^{13} \Delta t_{\rm obs,2}^{4/5} L_{\rm ssc,48}^{1/5} \ {\rm cm} \tag{15}$$

The distance from the black hole, in units of the Schwarzschild radius is

$$\frac{d}{R_{\rm S}} < 833 \frac{\Delta t_{\rm obs,2}^{4/5} L_{\rm ssc,48}^{1/5}}{\theta_{-1} M_6} \tag{16}$$

2.3.3 Modeling Procedure and Related Considerations

We use the blazar model described in detail in Ghisellini et al.[78] We assume a spherical emitting region of size R, moving with a bulk Lorentz factor Γ and located at a distance d from the black hole of mass M. The bolometric luminosity of the accretion disk is $L_{\rm disk}$.

The particle energy distribution, $N(\gamma)$ cm^{-3}, is calculated by solving the continuity equation, where particle injection, radiative cooling and pair production (via the γ–$\gamma \rightarrow e^{\pm}$ process) are taken into account. The created pairs contribute to the emission. The injection function, $Q(\gamma)$ cm^{-3} s^{-1}, is assumed to be a smoothly joined broken power-law, with slopes $Q(\gamma) \propto \gamma^{-s_1}$ and γ^{-s_2} below and above a break energy $\gamma_{\rm b}$:

$$Q(\gamma) = Q_0 \frac{(\gamma/\gamma_{\rm b})^{-s_1}}{1+(\gamma/\gamma_{\rm b})^{-s_1+s_2}} \tag{17}$$

In the specific application here, we assumed that electrons below a given γ_0 simply disappear.

The total power injected into the source in the form of relativistic electrons is $P'_{\rm i} = m_{\rm e} c^2 V \int Q(\gamma) \gamma d\gamma$, where $V = (4\pi/3) R^3$ is the volume of the emitting region.

The injection process lasts for a light crossing time R/c, and we calculate $N(\gamma)$ at this time. This assumption comes from the fact that even if injection lasted longer, adiabatic losses caused by the expansion of the source (which is travelling while emitting) and the corresponding decrease of the magnetic field would make the observed flux decrease. Therefore the computed spectra correspond to the maximum of a flaring episode.

Above and below the inner parts of the accretion disk there is an X-ray emitting corona of luminosity $L_{\rm X}$ (it is fixed at a level of 30% of $L_{\rm d}$). Its spectrum is a power law of energy index α_X ending with a exponential cutoff at $E_{\rm c}$ =150 keV. The specific energy density (i.e., as a function of frequency) of the disk and the corona are calculated in the comoving frame of the emitting blob, and used to properly calculate the resulting external inverse Compton spectrum. The internally produced synchrotron emission is used to calculate the synchrotron self Compton (SSC) flux. In this specific case we assume no Broad Line Region; the disk and the coronal radiation are negligible if the emitting region is at a large distance from the disk, but they become important producers of seed photons if the distance d of the emitting blob from the disk is of the same order of (or less than) the outer radius of the disk.

2.4 SED Modeling Input Parameters

Here we list model parameters used to produce the three models discussed in Supplementary Information §§2.5, 2.6, and 2.7. Supplementary Table 12 lists three sets of input parameters adopted to generate these three different models:

- Model 1: a magnetically-dominated jet produced by a 10^6 M$_\odot$ black hole with a constant luminosity accretion disk (our preferred model, discussed in SI§2.5),
- Model 2: a magnetically-dominated jet produced by a 10^7 M$_\odot$ black hole in which the jet luminosity tracks the accretion rate (discussed in SI§2.6), and
- Model 3: a particle-dominated jet produced by a 10^7 M$_\odot$ black hole (SI§2.7).

In Supplementary Figures 15 – 17 we show the models resulting from these input parameters.

Supplementary Table 12 | Input parameters used to model the SED. Col. [1]: Flux state: High (early flares), Low (low flux period between 4 and 9 days after the first BAT trigger), and Large (large radius emission region responsible for producing the observed radio flux); Col. [2]: size of the emitting region, in units of 10^{15} cm; Col. [3]: black hole mass in solar masses; Col. [4]: Disk luminosity in units of 10^{45} erg s^{-1} ; Col. [5]: $L_{\rm d}/L_{\rm Edd}$; Col. [6]: power injected in the blob calculated in the comoving frame, in units of 10^{45} erg s^{-1}; Col. [7]: magnetic field in Gauss; Col. [8]: bulk Lorentz factor; Col. [9]: viewing angle in degrees; Col. [10]: Doppler factor; Col. [11], [12] and [13]: minimum, break and maximum random Lorentz factors of the injected electrons; Col. [14] and [15]: slopes of the injected electron distribution [$Q(\gamma)$] below and above $\gamma_{\rm b}$; Col. [16] $\Delta t_{\rm v} \equiv R(1+z)/(c\mathscr{D})$. The disk has an X-ray corona of luminosity $L_X = 0.3L_{\rm d}$. The spectral shape of the corona is assumed to be $\propto \nu^{-1}\exp(-h\nu/150\ {\rm keV})$ for the models in Supplementary Figure 15 and Supplementary Figure 17, whilst it is $\propto \nu^{-0.7}\exp(-h\nu/150\ {\rm keV})$ in Supplementary Figure 16.

Flux State [1]	R [2]	M [3]	$L_{\rm d}$ [4]	$L_{\rm d}/L_{\rm Edd}$ [5]	$P'_{\rm i}$ [6]	B [7]	Γ [8]	$\psi_{\rm v}$ [9]	$\mathscr{D}$ [10]	γ_0 [11]	$\gamma_{\rm b}$ [12]	$\gamma_{\rm max}$ [13]	s_1 [14]	s_2 [15]	$\Delta t_{\rm v}$ [16]
Model 1: Supplementary Figure 15, SI§2.5															
High	0.03	1e6	0.13	1	0.15	3642	10	3	15.7	700	7e3	1e5	0.	2.2	86 s
Low	0.03	1e6	0.13	1	1.2e-2	3642	10	3	15.7	600	800	900	0	4.2	86 s
Large	27	1e6	0.13	1	1e-6	2.1	19	2	26.3	40	200	400	2.5	3.5	12.8 h
Model 2: Supplementary Figure 16, SI§2.6															
High	0.048	1e7	45	30	0.048	6014	12	2	20.4	500	9e3	4e4	0	2.4	106 s
Low	0.048	1e7	0.6	0.4	2.7e-3	694	12	2	20.4	1e3	1e3	2.5e3	0	2.8	106 s
Large	18	1e7	1.3	1	2e-6	2.1	17	2	25.1	10	100	300	0	2.0	8.9 h
Model 3: Supplementary Figure 17, SI§2.7															
High	0.036	1e7	1.3	1	0.18	60	13	2	21.5	1	60	80	2.5	3	75 s
Low	0.036	1e7	1.3	1	0.06	60	5	2	9.6	1	1	100	8	8	210 s

Supplementary Table 13 | Jet power in the form of radiation, Poynting flux, bulk motion of electrons and protons (assuming one proton per emitting electron). See Supplementary Table 12 for explanation of the flux states.

Flux State	$\log P_{\rm r}$	$\log P_{\rm B}$	$\log P_{\rm e}$	$\log P_{\rm p}$	$L_{0.3-10}/L_{tot}$	L_{15-150}/L_{tot}
Model 1: Supplementary Figure 15, SI§2.5						
High	46.12	45.65	41.07	41.05	0.216	0.318
Low	44.33	45.65	40.13	40.55	0.630	1.20e-6
Large	40.82	45.65	41.02	42.43	–	–
Model 2: Supplementary Figure 16, SI§2.6						
High	45.78	46.65	40.24	40.34	0.218	0.354
Low	44.03	44.78	40.77	40.95	0.512	8.5e-7
Large	41.30	45.17	41.31	42.71	–	–
Model 3: Supplementary Figure 17, SI§2.7						
High	46.14	42.47	44.71	47.74	0.098	0.175
Low	44.17	41.64	43.98	47.19	0.695	0.038

Supplementary Table 13 lists the power carried by the jet in the form of radiation ($P_{\rm r}$), magnetic field ($P_{\rm B}$), emitting electrons ($P_{\rm e}$, no cold electron component is assumed) and cold protons ($P_{\rm p}$, assuming one proton per emitting electron). All the powers are calculated as

$$P_i = \pi R^2 \Gamma^2 \beta c U_i' \tag{18}$$

where U_i' is the energy density of the i component, as measured in the comoving frame. We note the following regarding Supplementary Table 13:

- The power carried in the form of radiation, $P_{\rm r} = \pi R^2 \Gamma^2 \beta c U_{\rm rad}'$, can be rewritten, using $U_{\rm rad}' = L'/(4\pi R^2 c)$, as:

$$P_{\rm r} = L' \frac{\Gamma^2}{4} = L \frac{\Gamma^2}{4\mathscr{D}^4} \sim L \frac{1}{4\mathscr{D}^2} \tag{19}$$

  where L is the total observed non-thermal luminosity (L' is in the comoving frame) and $U_{\rm rad}'$ is the radiation energy density produced by the jet (i.e. excluding the external components). The last equality assumes $\psi_{\rm v} \sim 1/\Gamma$.

- When calculating $P_{\rm e}$ (the jet power in bulk motion of emitting electrons) we include their average energy, i.e. $U_{\rm e}' = n_{\rm e} \langle \gamma \rangle m_{\rm e} c^2$.

- For $P_{\rm p}$ (the jet power in bulk motion of cold protons) we have assumed that there is one proton per emitting electron, i.e. electron-positron pairs are negligible. This is unimportant for the models shown in Supplementary Figure 15 and 16, since in these cases the mean energy of the electrons is comparable to the rest mass of protons ($\langle \gamma \rangle m_{\rm e} \approx m_{\rm p}$). However, for the model shown in Supplementary Figure 17, $P_{\rm p}$ is the dominant form of power.

- $P_{\rm B}$ is derived using the magnetic field found from the model fitting.

In summary, we have studied the extreme cases of a jet whose power is largely dominated by the magnetic field (Models 1,2; Supplementary Figures 15 and 16) or by the kinetic energy of the matter (Model 3; Supplementary Figure 17).

2.5 SED Model 1: A magnetic field-dominated jet from a 10^6 $M_\odot$ black hole

Since the accretion can be super-Eddington, the density of the accreting matter is large and can sustain a very large B-field, which launches the jet. In the dissipation region, the B-field is still large, possibly because it has not completed the acceleration of the matter. Dissipation can occur at the expense of the magnetic field, through reconnection.

Rationale — The photons we observe in the K band started in the H band in the transient rest frame, and we have $A_H \sim 0.175 A_V$. Therefore, even if the A_V is underestimated, the point in K would not move much. Thus the $\nu^{1/3}$ slope between the IR and the X-rays is solid. This $\nu^{1/3}$ slope can be a coincidence, or it can indicate the presence of a synchrotron tail produced by an electron distribution with a low energy cut-off.

We first consider the scenario in which **NIR and X-ray are produced by the same synchrotron emission component.** In this case, we have: i) a very large synchrotron luminosity and ii) electrons that cannot cool below a given energy, even though the variability indicates a compact source, where the cooling is very rapid (i.e. much much less than the light crossing time R/c). Since all the emitting electrons have large energies, we do not need many of them to produce the radiation we see. This means that the source is "particle starved". A corollary: since the electrons could have $\langle\gamma\rangle \gtrsim 10^3$, it is not important whether or not we have a proton per emitting electron.

Consider also that the jet must have more power than the radiation it produces. We have that:

- The emitting electrons and their associated protons do not carry much kinetic power
- We need something to keep the electrons hot (i.e. they cannot cool below – say – $\gamma = 10^3$).
- The synchrotron luminosity is large (if the X-rays are synchrotron)

These conditions lead us to prefer a Poynting-dominated jet, because reconnection can keep the electrons hot and all the emission can be done with few particles.

Some numbers (synchrotron case) — Assume that the X-rays are produced by a particle distribution $N(\gamma) \propto \gamma^{-p}$ between γ_1 and γ_2. Assume also that $n_e \equiv \int N(\gamma) d\gamma$. With this distribution we can calculate $\langle\gamma\rangle$ and $\langle\gamma^2\rangle$. In particular the Comptonization parameter y is

$$y \equiv \sigma_T n_e R \langle\gamma^2\rangle \tag{20}$$

The rest frame synchrotron frequency corresponding to γ_1 is

$$\nu_1 = \frac{4}{3}\frac{eB}{2\pi m_e c^2}\gamma_1^2 B\mathscr{D} = 3.6\times 10^6 \gamma_1^2 B\mathscr{D} \tag{21}$$

The energy density of the synchrotron radiation can be written as:

$$\begin{aligned} U'_{\rm syn} &= \frac{L'_{\rm syn}}{4\pi R^2 c} = \frac{4\pi R^3}{3}\frac{\int N(\gamma)\dot{\gamma}_{\rm syn} m_e c^2 d\gamma}{4\pi R^2 c} \\ &= \frac{4\pi R^3}{3}\frac{4}{3}\frac{n_e \sigma_T c \langle\gamma^2\rangle U_B}{4\pi R^2 c} = \frac{4}{9} R n_e \sigma_T \langle\gamma^2\rangle U_B = \frac{4}{9} y U_B \end{aligned} \tag{22}$$

where y is the Comptonization parameter. Therefore we can write:

$$\frac{L^{\rm obs}_{\rm syn}}{4\pi R^2 c \mathscr{D}^4} = \frac{4}{9} y U_B \rightarrow U_B = \frac{9 L^{\rm obs}_{\rm syn}}{16\pi \mathscr{D}^4 y R^2 c} \tag{23}$$

The particle energy density is

$$U'_e = n_e \langle\gamma\rangle m_e c^2 = \frac{y m_e c^2}{\sigma_T R}\frac{\langle\gamma\rangle}{\langle\gamma^2\rangle} \tag{24}$$

Therefore (setting $R = c\Delta t_{\rm v}\mathscr{D}$):

$$\frac{U_B}{U'_e} = \frac{9 L_{\rm syn}}{16\pi y^2 c^2 \Delta t_{\rm v} \mathscr{D}^5}\frac{\langle\gamma^2\rangle}{\langle\gamma\rangle}\frac{\sigma_T}{m_e c^2} \tag{25}$$

For $2 < p < 3$, the ratio

$$\frac{\langle\gamma^2\rangle}{\langle\gamma\rangle} = \frac{p-2}{3-p}\frac{\gamma_2^{3-p}}{\gamma_1^{2-p}} \tag{26}$$

For $p = 2.5$ this simplifies to $\langle\gamma^2\rangle/\langle\gamma\rangle = (\gamma_2\gamma_1)^{1/2}$.

Setting $\Delta t_{\rm v} = 10^2\Delta t_{\rm v,2}$, $\mathscr{D} = 10\mathscr{D}_1$, $L_{\rm syn}^{\rm obs} = 10^{48}L_{48}$, and setting $p = 2.5$ we have

$$\frac{U_B}{U'_e} = 16.1\frac{L_{48}}{\Delta t_{\rm v,2}\mathscr{D}_1^5}\frac{(\gamma_1\gamma_2)^{1/2}}{y^2} \tag{27}$$

As an estimate for $(\gamma_1\gamma_2)^{1/2}$, we have

$$(\gamma_1\gamma_2)^{1/2} = 7.46\times10^4\left(\frac{\nu_{1,17}\nu_{2,19}}{U_B\mathscr{D}_1^2}\right)^{1/4} = 2.6\times10^3\,\mathscr{D}_1\left(\frac{y\Delta t_{\rm v,2}^2\nu_{1,17}\nu_{2,19}}{L_{48}}\right)^{1/4} \tag{28}$$

Giving

$$\frac{U_B}{U'_e} = 4.2\times10^4\frac{L_{48}^{3/4}}{\Delta t_{\rm v,2}^{1/2}\mathscr{D}_1^4}\frac{(\nu_{1,17}\nu_{2,19})^{1/4}}{y^{7/4}} \tag{29}$$

The magnetic field is

$$B = \left(\frac{9L_{\rm syn}^{\rm obs}}{2y\mathscr{D}^6c^3\Delta t_{\rm v}^2}\right)^{1/2} = \frac{4\times10^3}{\mathscr{D}_1^3\Delta t_{\rm v,2}}\left(\frac{L_{48}}{y}\right)^{1/2}\ \text{Gauss} \tag{30}$$

and the minimum electron energy γ_1 is

$$\gamma_1 = \left(\frac{\nu_1}{3.6\times10^6B\mathscr{D}}\right)^{1/2} = \left(\frac{\nu_1}{3.6\times10^6B\mathscr{D}}\right)^{1/2} = 1.67\times10^3\left(\frac{\nu_{1,17}}{B_3\mathscr{D}_1}\right)^{1/2} \tag{31}$$

The jet power in Poynting flux is

$$P_B = \pi R^2\Gamma^2cU_B = \frac{9}{16}\frac{\Gamma^2}{\mathscr{D}^4}\frac{L_{\rm syn}^{\rm obs}}{y} = 5.6\times10^{45}\frac{\Gamma_1^2}{\mathscr{D}_1^4}\frac{L_{48}^{\rm obs}}{y} \tag{32}$$

The power spent in the form of radiation is

$$P_{\rm r} = \pi R^2\Gamma^2cU'_r = \frac{\Gamma^2}{4\mathscr{D}^4}L_{\rm syn}^{\rm obs} = 2.5\times10^{45}\frac{\Gamma_1^2}{\mathscr{D}_1^4}L_{48}^{\rm obs} \tag{33}$$

Since $P_{\rm jet}\sim P_B$ must be larger or equal to $P_{\rm r}$, the Comptonization parameter y cannot be too large.

We consider two variations of model parameters within this basic magnetically-dominated model. Both rely on the SSC process (the magnetic energy density dominates over the radiation energy density of external seed photons; see Table 13), but adopt different black hole masses: 10^6 $M_\odot$ and 10^7 $M_\odot$, respectively. In Model 1, shown in Supplementary Figures 15, the disk luminosity is kept constant at the Eddington value, even if the jet luminosity and its power change. As can be seen, the disk luminosity can barely contribute to the soft X-ray flux.

The dotted orange line in both models shows the flux emitted from a much larger region of the jet that produces the radio flux (generated in an external shock with the surrounding medium).

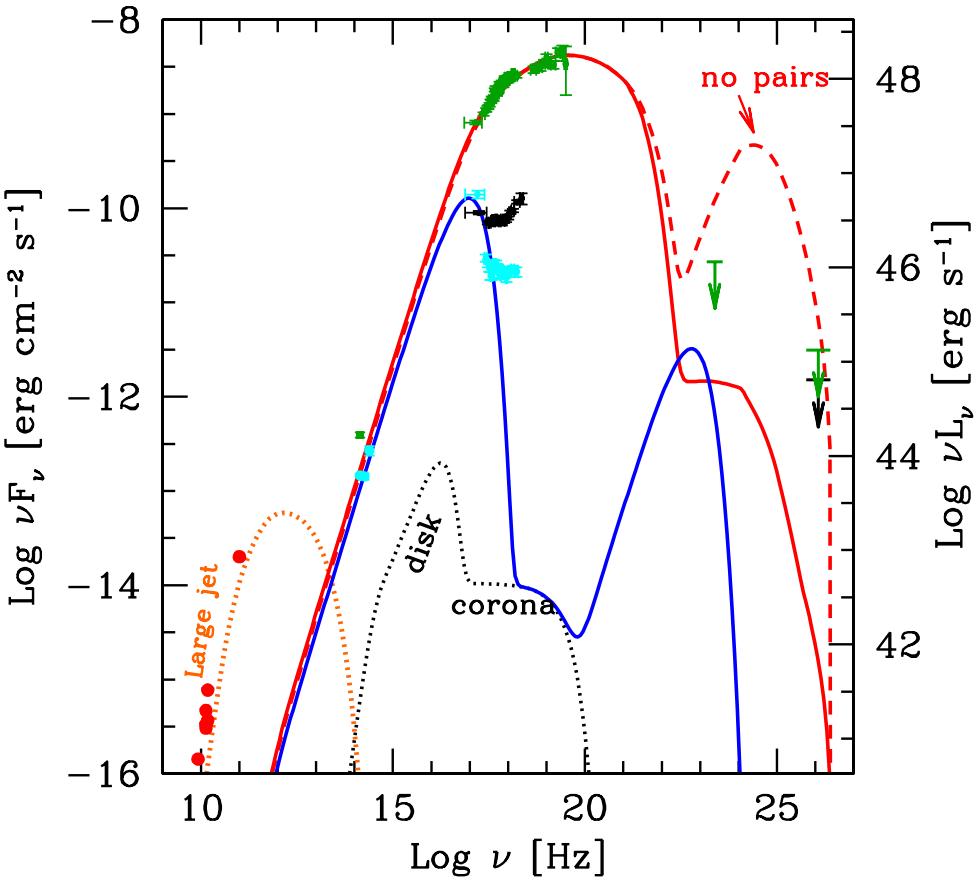

Supplementary Figure 15 | Spectral Energy Distribution for Sw J1644+57. The green data points show the SED from the early bright flaring phase; cyan data points are from the low state at ~ 4.5 days; black data points are from roughly 8 days after the first BAT trigger. In the NIR, this includes a Ks band point 48 hours after the trigger (green); and J, H, and Ks band fluxes 4.5 days after trigger (cyan). The NIR flux has been dereddened with $A_V = 4.5$. In the X-ray band we show the spectrum at the peak of the bright flares (31 hours after first BAT trigger; XRT and BAT; green) and in the low flux state (~ 4.5 days after, XRT only; cyan), together with the spectrum in the intermediate persistent flux state that began a week after the first BAT trigger (time integrated between day 6.5 and 9.5 from trigger, XRT only; black). The X-ray data have been corrected for absorption with a constant $N_H = 2 \times 10^{22}$ cm^{-2}. Upper limits from the *Fermi* LAT at 2×10^{23} Hz and from *VERITAS* at 10^{26} Hz[75] are also shown. The red curve shows the model discussed in the text, which is a blazar jet model[78] fit to our SED during the bright, early X-ray flares. The dominant emission mechanism is synchrotron radiation peaking in the X-ray band. On the low frequency side, the hard slope between the NIR and X-ray bands requires suppression of low-energy electrons, which would otherwise overproduce the NIR flux. On the high frequency side, the LAT and *VERITAS* upper limits require that the self-Compton component is suppressed by γ–γ pair production, without which the model would follow the dashed curve and would significantly overproduce the GeV and TeV emission. The model includes a disk/corona component from the accretion disk (black dotted curve), but the flux is dominated at all frequencies by the synchrotron component from the jet. The blue curve shows the corresponding model in the low X-ray flux state. The model was fit to the NIR and X-ray data, and fits the low energy X-ray data well. The kink in the X-ray spectrum suggests a possible additional component may be required; it would have to be very narrow, and its origin is unclear. In the low state the Inverse Compton component is below the LAT and *Fermit* upper limits without the need for further suppression at high energies. The black data points show the X-ray spectrum at an intermediate flux state, for comparison with the high and low flux state SEDs. We have not attempted to fit the SED at this epoch. The radio fluxes come from a larger region of the jet (orange dotted line). See Supplementary Tables 12 and 13 for the model parameters of this fit.

2.6 SED Model 2: A magnetically-dominated jet from a 10^7 $M_\odot$ black hole

The SED produced by Model 2 is shown in Figure 16. Model 2 is very similar to the Model 1, but explores a different set of input parameters. Both models rely on the SSC process (the magnetic energy density dominates over the radiation energy density of external seed photons), but adopt different black hole masses: 10^6 $M_\odot$ and 10^7 $M_\odot$, respectively.

Here we have increased the black hole mass from $M_6 = 1$ (Model 1) to $M_6 = 10$ (Model 2). For Model 2 we have assumed that the jet luminosity tracks a rapidly varying accretion luminosity. In this case, we have assumed a super-Eddington luminosity for the high state, and nearly Eddington for the low state. As can be seen, the disk luminosity can barely contribute to the soft X-ray flux.

Like Model 1, this model is also dominated by the energy of the magnetic field (see Table 13).

The dotted orange line in both models shows the flux emitted from a much larger region of the jet, producing the radio flux.

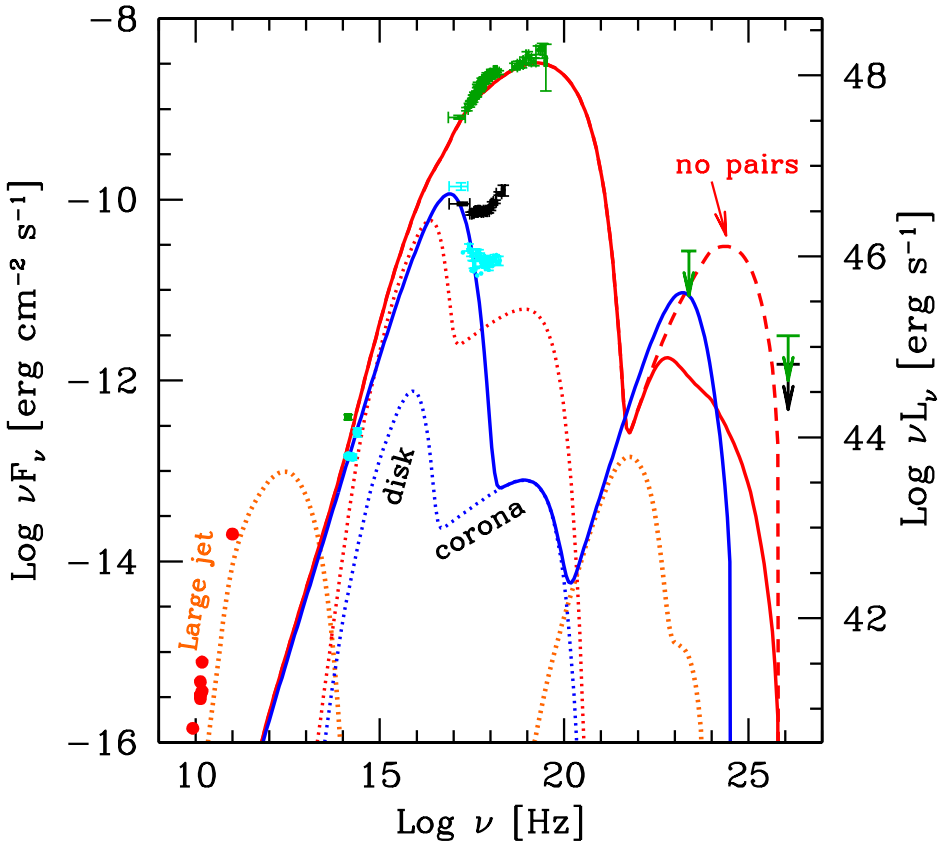

Supplementary Figure 16 | Data as in Supplementary Figure 15. Here the model is similar to that shown in Supplementary Figure 15, but the black hole mass is larger ($M_{\rm bh} = 10^7$ $M_\odot$), and the jet luminosity is assumed to approximately track a changing disk luminosity, from 30×Eddington in the high state to 0.6×Eddington in the low state (dotted lines). The basic features of the jet are similar to the previous case, but the Poynting flux is not constant, instead it tracks $\dot{M}$.

2.7 SED Model 3: A matter-dominated jet

The alternative to the assumption that the NIR and X-ray photons are produced in the same emission region is to argue that the $\nu^{1/3}$ slope between the NIR to X-ray bands is a coincidence, and the "jump" between these bands is due to a very, very large U'_{ext}/U_B, similar to an extremely powerful blazar (but in this case it is more extreme – note that in the model of Bloom et al.[76], which takes this approach, they fit the *low* X-ray state, whereas we are fitting the *high* X-ray state, a factor of ~ 100 more luminous). This matter-dominated jet can also reproduce the observed SED (Supplementary Figure 17), but only under rather extreme conditions. For this model we assume that even if, at the start, the jet is dominated by the magnetic field, nevertheless the Poynting flux is able to accelerate the jet to its final bulk Lorentz factor, Γ, before the dissipation region. The jet then becomes dominated by the kinetic energy of matter (Supplementary Table 13); therefore dissipation is at the expense of the latter, as in all other blazars. In this case the IR is synchrotron, and the X-rays are external Compton (since it is very difficult to produce such a jump with the SSC model). A source of external photons is required, and the most obvious source of these seed photons is the accretion disk. This model requires an accretion disk with an outer radius of $\gtrsim 300$ Schwarzschild radii, since the upscattered photons must enter the jet with a substantial angle in order for the Compton scattering to be efficient (the accretion disk radius is 500 R_S for the model shown in Supplementary Figure 17). Model 3 is similar to models used for blazars, but with a particle energy distribution that does not extend up to such large energies (i.e. $\gamma_{max} \sim 80 - 100$), and with most of the electrons at low energies. Therefore in this case we have a sort of bulk-Compton process, in which relatively cold electrons scatter the seed photons coming from the outer radius of the disk. Model 3 is similar to the one presented by Bloom et al.[76], but in our case the IR and X-ray photons are produced in the same region. The large L_X/L_{IR} ratio is due to the large ratio between the energy densities of the external radiation and the magnetic field. This requires a small magnetic field, and therefore a matter-dominated jet.

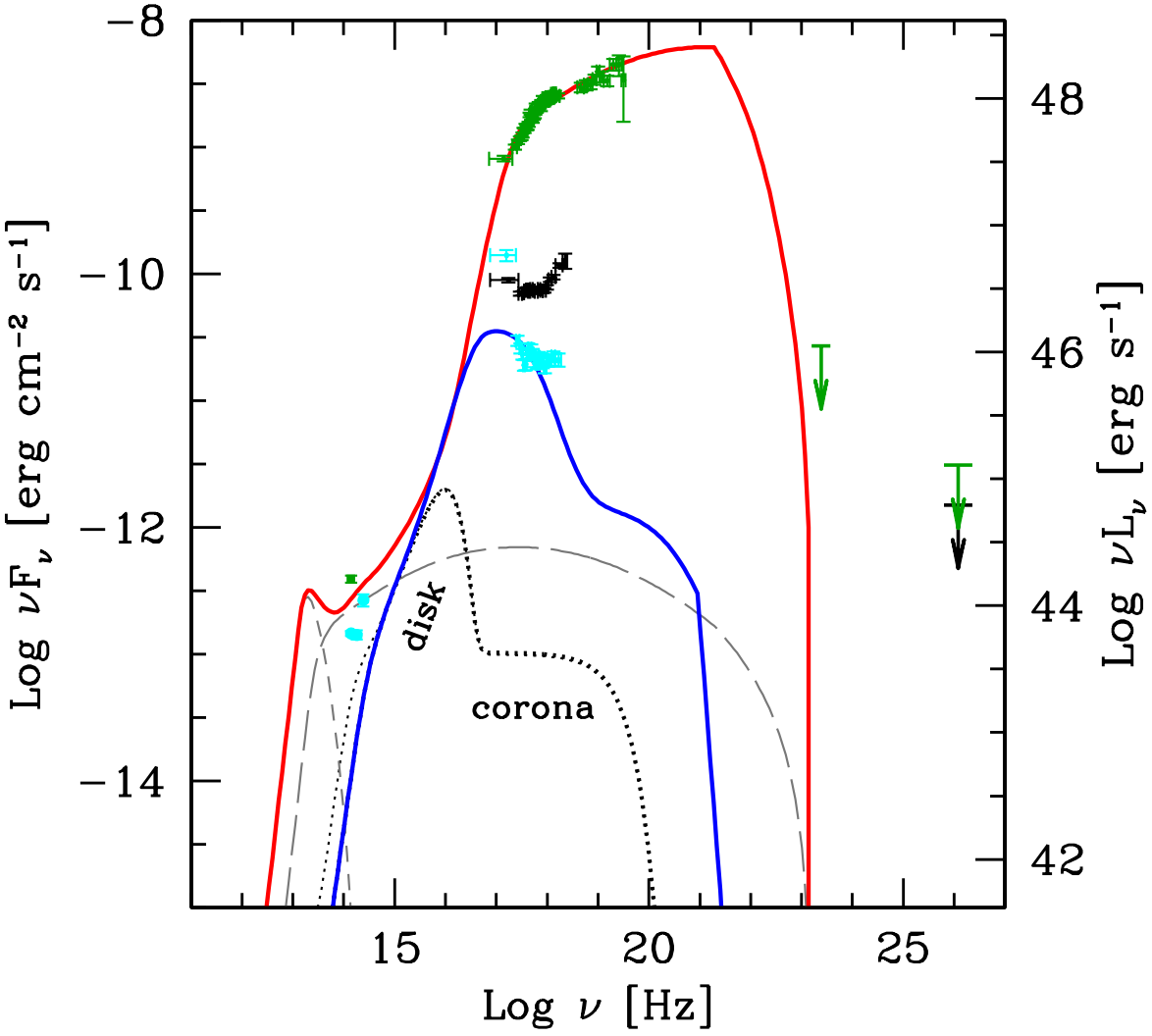

Supplementary Figure 17 | Data as in Supplementary Figure 15. In this model the NIR flux is synchrotron radiation, and the X-rays are produced by the external Compton. The model assumes a matter-dominated jet whose dissipating region is very close to the accretion disk (i.e. 120 R_S, the black hole mass is assumed to be $10^7 M_\odot$). The disk itself is assumed to extend out to ~500 R_S. In this case the external part of the disk produces IR photons that can be efficiently scattered by the relativistic electrons in the jet. In order to avoid overproducing the NIR, the magnetic field is small, and the jet is therefore matter-dominated. The high state (red line) and the low state (blue line) differ in the amount of injected power in relativistic electrons and in the bulk Lorentz factor. The short-dashed gray line is the synchrotron flux in the high state, whilst the long-dashed line is the corresponding SSC component.

2.8 Magnetically-dominated jet within a GRB model

We can also treat J1644+57 within the context of the standard GRB internal shock model. This shows that a completely different modeling approach comes to similar conclusions regarding the relative importance of magnetic fields and particles in this jet.

We adopt the following parameters:

- The ejecta wind luminosity (including kinetic, magnetic field and radiation) is $L_w = 10^{48}$ erg s$^{-1} L_{48}$.
- Bulk Lorentz factor is $\Gamma = 100\Gamma_2 = 100$, which is a typical value for GRBs.
- Variability time scale is $\Delta t_{\rm v} = 100$ s$\Delta t_{\rm v,2}$ (we ignore the redshift correction here).

We introduce 3 parameters:

1. A fraction ε_B of the total wind energy that goes to magnetic fields. Here we combine the traditional definition of ε_B and the internal random Lorentz factor, which is of order unity. There might also be a global B field entrained from the ejecta.
2. A fraction ε_e of the internal energy that goes to electrons.
3. A fraction ξ_e of the total electrons that are accelerated. This parameter describes whether the flow is "particle starved" in the context of the discussion in SI§2.5.

In the internal shock synchrotron model, the spectral slope is $1/3$ below both ν_m and ν_c. In order to interpret the data (the $1/3$ slope from optical to X-rays), we require that

$$\nu_{\rm X} < \min(\nu_m, \nu_c) \ . \tag{34}$$

With the adopted parameters, the lab frame magnetic field strength can be estimated by $B^2/8\pi \sim \varepsilon_B L_w/4\pi R^2 c$. So the comoving magnetic field strength is

$$B' \sim 2.7 \ {\rm G} \ \varepsilon_B^{1/2} L_{48}^{1/2} \Gamma_2^{-3} \Delta t_{\rm v,2}^{-1} \ . \tag{35}$$

The "cooling" Lorentz factor at $\Delta t_{\rm v} \sim 100$ s is

$$\gamma_c = \frac{6\pi m_e c}{\sigma_{\rm T} B'^2 \Gamma \Delta t'} \sim 1.0 \times 10^4 \Gamma_2^5 L_{48}^{-1} \varepsilon_B^{-1} \Delta t_{\rm v,2} \ , \tag{36}$$

This gives the cooling frequency

$$\nu_c = \Gamma \frac{3}{4\pi} \gamma_c^2 \frac{eB'}{m_e c} \sim 1.2 \times 10^{17} \ {\rm Hz} \Gamma_2^8 L_{48}^{-3/2} \varepsilon_B^{-3/2} \Delta t_{\rm v,2} \ . \tag{37}$$

This is in the X-ray band. Noticing the sensitive dependence on Γ, a small increase in the bulk Lorentz factor will put ν_c above the X-ray band. The large bulk Lorentz factor results in high γ_c and ν_c, and also results in a large internal shock radius $R_{\rm IS} \sim \Gamma^2 c \Delta t_{\rm v} = 3 \times 10^{16}$ cm$\Gamma_2^2 \Delta t_{\rm v,2}$. The magnetic field strength at this radius is very low (eq.[35]), so that synchrotron cooling is not significant.

In order to have ν_m to be at least greater than ν_c, one requires that the minimum injection electron Lorentz factor $\gamma_m \geq \gamma_c$. This Lorentz factor can be estimated as

$$\gamma_m \sim \left(\frac{\varepsilon_e}{\xi_e}\right)\left(\frac{p-2}{p-1}\right)\left(\frac{m_p}{m_e}\right)\theta \sim 310 \left(\frac{\varepsilon_e}{\xi_e}\right)\theta \ , \tag{38}$$

where θ is the internal random Lorentz factor in the internal shock, which is of order unity. One can see that in order to have $\gamma_e \geq 10^4$, one requires $\xi_e \ll 1$, so that $\varepsilon_e/\xi_e \geq 30$. As a result, we obtain the same result with the GRB model

as obtained in SI§2.5, namely, the emission region is "particle starved" even within the internal shock fast cooling scenario.

The most straightforward inference is that the outflow is Poynting flux dominated. A Poynting flux dominated outflow also eases the requirement of launching a highly collimated jet from a newly activated massive black hole. Alternatively, the data may be interpreted within the fireball internal shock model, if only a small fraction of electrons can be accelerated in internal shocks. In any case, the outflow has to be "particle starved".

2.9 Two Models for Jet Onset

Our observations of Sw J1644+57 provide strong evidence for the onset of a relativistic jet powered by accretion onto a massive black hole. Accretion of matter onto massive black holes provides the power for active galactic nuclei (AGNs). However, not all massive black holes are associated with AGNs, and this implies that AGNs turn off when the accretion rate becomes very low. Sgr A*, the massive black hole in the centre of our Milky Way galaxy, is a nearby example. Sgr A* has a mass of $\sim 4\times10^6 M_\odot$ [79,80], and yet has a quiescent soft X-ray luminosity [81,82] of only 4×10^{32} erg s^{-1}, which would be undetectable at z=0.354.

We expect that AGNs can also turn on again if they become reactivated by a new supply of accreting material. This could be a single stellar capture (a tidal disruption event) or a more long-lived gas source such as an interstellar cloud, SN ejecta, or stellar winds. Here we discuss two physical scenarios that could be responsible for the observed jet onset: tidal disruption of a main sequence star, and onset of an AGN. Observationally, these are primarily distinguished by the expected timescales of the activity.

2.9.1 Tidal Disruption Event

This luminous, accretion-powered, relativistic jet is likely initiated by the tidal disruption of a star [69,83,84,85,86,87,88], where we cite only a small fraction of the substantial literature on this subject. A dormant black hole can be activated by capturing the remnants of a star disrupted in its strong graviational field. The vast majority of papers on tidal disruption events (TDEs) have concentrated on the expected emission from the initial crushing of the star during its pericenter passage [89,86,88], emission from the accretion disk [84,85,87], or emission from a wind outflow [87], but it is natural that a TDE might also produce a jet [90,87] like those produced by accretion onto objects ranging from neutron stars (such as the Crab pulsar) and stellar mass black holes (e.g., GRS 1915+105) to supermassive black holes in blazars. The jet dominates the observed emission in Sw J1644+57.

If Sw J1644+57 is the manifestation of a tidal disruption event (TDE), we can estimate the jet collimation (or beaming factor) based on the rate of TDEs in the local universe. The *Swift* BAT, with a field of view of $\sim 4\pi/7$ sr, has detected one such event in ~ 6 years at a peak flux that would have been detectable to $z\sim0.8$. The all-sky rate of Sw J1644+57-like events is therefore $R_{4\pi}\sim1$ yr^{-1}, with a 90% confidence interval [56] of $0.08-3.9$ yr^{-1}. The rate of tidal disruption events is thought to be $\sim10^{-5}$ yr^{-1} galaxy^{-1} on both observational [91,92] and theoretical [93] grounds. Given the galaxy number density $n_{\rm gal}\sim0.01$ Mpc^{-3}, the total number of galaxies in the co-moving volume within $z<0.8$ can be estimated as $N_{\rm gal}(z<0.8)\sim10^9$. This gives a total tidal disruption event rate of $R_{\rm TD,4\pi}(z<0.8)\sim10^4$ yr^{-1}. If these act like AGN, 10% of them contain relativistic ("radio-loud") jets. The fraction of these jets that point towards us is

$$\max\left(\frac{1}{2\Gamma^2},\frac{\theta_j^2}{2}\right),$$

where Γ is the bulk Lorentz factor and θ_j is the opening angle of the jet. A bulk Lorentz factor of $\Gamma\sim10-20$ or a jet opening angle of $\theta_j\sim5^\circ$ would provide the observed event rate. Since we also require $\Gamma\sim10$ in order to suppress the high energy γ-rays in our preferred model, this relativistic jet self-consistently accounts for both the SED and the event rate. Our observations are consistent with theoretical predictions of the formation of a low-density, magnetically-dominated jet during the super-Eddington phase of a tidal disruption event around a $10^6-10^7 M_\odot$ black hole [87].

In the tidal disruption interpretation, we expect the source to begin a slow decay once the material in the accretion disk is exhausted and the luminosity begins to track the fall-back timescale ($t^{-5/3}$) of the disrupted stellar material onto the black hole [94]. Theoretical predictions suggest that the timescale for this $t^{-5/3}$ fallback of material onto the accretion disk to begin may be months [84,94]. The observed light curve may not track this decay rate, though, due to spectral evolution [95], resulting in very different predicted light curve shapes that do not even follow power laws. On the other hand, Krolik and Piran [96] argue that the variability timescales in the X-ray light curve of Sw J1644+57 provide evidence for tidal disruption of a white dwarf onto an intermediate mass black hole ($M\sim10^4 M_\odot$), rather than the main sequence stellar disruption by a more massive black hole envisioned in most of the theoretical work cited above. In this case, all timescales are orders of magnitude shorter, and the $t^{-5/3}$ fallback may begin within days after the initial pericenter passage. We note that the overall X-ray decay for the first 50 days can be fit roughly as a $t^{-5/3}$

decay (ignoring the dips), though as we pointed out in SI§1.1.2, the decay is not smooth and can also be modeled as a series of steps, so the fit to a power law decay is only approximate. However, over a longer time-scale of ~ 100 days since the first BAT trigger, the overall light curve decay appears to be nearly exponential (Supplementary Figure 2). Long-term monitoring of Sw J1644+57 will be necessary to determine the true decay behaviour, which may then shed further light on the details of the physical origin of this event.

2.9.2 AGN Onset

Although we consider that the tidal disruption model is the most likely explanation for the behaviour of Sw J1644+57, other types of accretion onset cannot be ruled out. Gas from steller winds or supernovae in a rotating galactic bulge could be captured in an accretion disk around the central supermassive black hole. The inner radius of this disk will decrease slowly under the effect of α viscosity, but as the inner radius approaches the innermost stable orbit the final infall timescale becomes $t_d \sim 2 \times 10^3 (\alpha/0.1)^{-1} M_6$ s, resulting in a rapid onset of electromagnetic radiation that is consistent with our observations of Sw J1644+57.

We can estimate the rate at which AGNs turn on as follows. We assume that the typical life time of an AGN is $t_{\rm AGN} \sim 3 \times 10^7$ yr. In steady-state, the rate at which AGN turn on is therefore $\sim t_{\rm AGN}^{-1}$. Within the $z < 0.8$ volume, the event rate of the onset of a new radio-loud AGN would be $R_{\rm AGN,tot} = 0.1 N_{\rm gal}(z < 0.8)/t_{\rm AGN} \sim 3$ yr^{-1}. A moderate Lorentz factor of $\Gamma \sim 3$ or an opening angle of $\theta_j \sim 13^\circ$ would have an event rate of ~ 0.1 yr^{-1}, consistent with the observations.

In the case of AGN onset one expects an extremely long-lived event ($\sim t_{\rm AGN}$). The long-term behaviour of Sw J1644+57 to date is a nearly monotonic decrease in flux, which favours the tidal disruption interpretation. Nevertheless, we expect that continued long-term monitoring of Sw J1644+57 will be required to distinguish between these scenarios for the accretion.

References

31. Gehrels, N. *et al.* The Swift Gamma-Ray Burst Mission. *Astrophys. J.* **611**, 1005–1020 (2004).

32. Barthelmy, S. D. *et al.* The Burst Alert Telescope (BAT) on the SWIFT Midex Mission. *Space Sci. Rev.* **120**, 143–164 (2005).

33. Cummings, J. R. *et al.* GRB 110328A: Swift detection of a burst. *GRB Coordinates Network, Circular Service* **11823** (2011).

34. Sakamoto, T. *et al.* GRB 110328A / Swift J164449.3+573451: BAT refined analysis. *GRB Coordinates Network, Circular Service* **11842** (2011).

35. Barthelmy, S. D. *et al.* GRB 110328A: a second trigger, probably a hard X-ray transient (Swift J164449.3+573451). *GRB Coordinates Network, Circular Service* **11824** (2011).

36. Burrows, D. N. *et al.* The Swift X-Ray Telescope. *Space Sci. Rev.* **120**, 165–195 (2005).

37. Vaughan, S. *et al.* Swift Observations of the X-Ray-Bright GRB 050315. *Astrophys. J.* **638**, 920–929 (2006).

38. Evans, P. A. *et al.* Methods and results of an automatic analysis of a complete sample of Swift-XRT observations of GRBs. *Mon. Not. R. Astron. Soc.* **397**, 1177–1201 (2009).

39. Pagani, C. *et al.* Recovering Swift-XRT energy resolution through CCD charge trap mapping. *Astron. Astrophys., submitted* (2011).

40. Roming, P. W. A. *et al.* The Swift Ultra-Violet/Optical Telescope. *Space Sci. Rev.* **120**, 95–142 (2005).

41. Poole, T. S. *et al.* Photometric calibration of the Swift ultraviolet/optical telescope. *Mon. Not. R. Astron. Soc.* **383**, 627–645 (2008).

42. Schlegel, D. J., Finkbeiner, D. P. & Davis, M. Maps of Dust Infrared Emission for Use in Estimation of Reddening and Cosmic Microwave Background Radiation Foregrounds. *Astrophys. J.* **500**, 525 (1998).

43. Levan, A. J. *et al.* An extremely luminous panchromatic outburst from the nucleus of a distant galaxy. *Science* **333**, 199 (2011). arXiv:1104.3356.

44. Han, W. *et al.* Development of a 1-m Robotic Telescope System. *Pub. Astr. Soc. of Japan* **57**, 821–826 (2005).

45. Lee, I., Im, M. & Urata, Y. First Korean Observations of Gamma-Ray Burst Afterglows at Mt. Lemmon Optical Astronomy Observatory (LOAO). *Journal of Korean Astronomical Society* **43**, 95–104 (2010).

46. Im, M. *et al.* Seoul NAtional University 4K x 4K Camera (SNUCAM) for Maidanak Observatory. *Journal of Korean Astronomical Society* **43**, 75–93 (2010).

47. Moon, B. *et al.* KASINICS: Near Infrared Camera System for the BOAO 1.8m Telescope. *Pub. Astr. Soc. of Japan* **60**, 849– (2008).

48. Baffa, C. *et al.* NICS: The TNG Near Infrared Camera Spectrometer. *Astron. Astrophys.* **378**, 722–728 (2001).

49. Stetson, P. B. DAOPHOT - A computer program for crowded-field stellar photometry. *Pub. Astr. Soc. of the Pacific* **99**, 191–222 (1987).

50. Pei, Y. C. Interstellar dust from the Milky Way to the Magellanic Clouds. *Astrophys. J.* **395**, 130–139 (1992).

51. Cenko, S. B., Nugent, P. E., Fox, D. B., Ofek, E. O. & Kasliwal, M. M. GRB 110328A / Swift J164449.3+573451: PTF Quiescent Optical Counterpart. *GRB Coordinates Network, Circular Service* **11827** (2011).

52. Matsuoka, M. *et al.* The MAXI Mission on the ISS: Science and Instruments for Monitoring All-Sky X-Ray Images. *Pub. Astr. Soc. of Japan* **61**, 999– (2009).

53. Mihara, T. *et al.* Gas Slit Camera (GSC) onboard MAXI on ISS. *Pub. Astr. Soc. of Japan,* in press (2011). arXiv:1103.4224.

54. Kimura, M. *et al.* MAXI/GSC observation of Swift J164449.3+573451. *The Astronomer's Telegram* **3244** (2011).

55. Israel, G. L. & Stella, L. A New Technique for the Detection of Periodic Signals in "Colored" Power Spectra. *Astrophys. J.* **468**, 369 (1996).

56. Kraft, R. P., Burrows, D. N. & Nousek, J. A. Determination of confidence limits for experiments with low numbers of counts. *Astrophys. J.* **374**, 344–355 (1991).

57. Saxton, R. D. *et al.* The first XMM-Newton slew survey catalogue: XMMSL1. *Astron. Astrophys.* **480**, 611–622 (2008).

58. Baumgartner, W. *et al.* . *Astrophys. J. Suppl, submitted* (2011).

59. Tueller, J. *et al.* The 22 Month Swift-BAT All-Sky Hard X-ray Survey. *Astrophys. J. Suppl* **186**, 378–405 (2010).

60. Cusumano, G. *et al.* The Palermo Swift-BAT hard X-ray catalogue. III. Results after 54 months of sky survey. *Astron. Astrophys.* **524**, A64 (2010).

61. Marconi, A. & Hunt, L. K. The Relation between Black Hole Mass, Bulge Mass, and Near-Infrared Luminosity. *Astrophys. J. (Letters)* **589**, L21–L24 (2003).

62. Leloudas, G. *et al.* GRB 110328A / Swift J164449.3+573451: NOT optical observations. *GRB Coordinates Network, Circular Service* **11830** (2011).

63. Fruchter, A. *et al.* GRB 110328A / Swift J164449.3+573451, HST Observations. *GRB Coordinates Network, Circular Service* **11881** (2011).

64. Gültekin, K. *et al.* The M-σ and M-L Relations in Galactic Bulges, and Determinations of Their Intrinsic Scatter. *Astrophys. J.* **698**, 198–221 (2009). 0903.4897.

65. Cenko, S. B. *et al.* GRB 110328A / Swift J164449.3+573451: Keck/DEIMOS Optical Spectroscopy. *GRB Coordinates Network, Circular Service* **11874** (2011).

66. Fukugita, M., Shimasaku, K. & Ichikawa, T. Galaxy Colors in Various Photometric Band Systems. *Pub. Astr. Soc. of the Pacific* **107**, 945 (1995).

67. Treu, T., Woo, J.-H., Malkan, M. A. & Blandford, R. D. Cosmic Evolution of Black Holes and Spheroids. II. Scaling Relations at z=0.36. *Astrophys. J.* **667**, 117–130 (2007).

68. Giannios, D., Uzdensky, D. A. & Begelman, M. C. Fast TeV variability in blazars: jets in a jet. *Mon. Not. R. Astron. Soc.* **395**, L29–L33 (2009).

69. Rees, M. J. Tidal disruption of stars by black holes of 10 to the 6th-10 to the 8th solar masses in nearby galaxies. *Nature* **333**, 523–528 (1988).

70. Bower, G., Bloom, J. S. & Cenko, B. Upper Limit on Radio Polarization for GRB 110328A / Swift J164449.3+573451. *The Astronomer's Telegram* **3278**, 1 (2011).

71. Pooley, G. GRB 110328A / Swift J164449.3+573451. *GRB Coordinates Network, Circular Service* **11849** (2011).

72. Castro-Tirado, A. J. *et al.* GRB 110328A / Swift J164449.3+573451: millimeter detection at PdBI. *GRB Coordinates Network, Cirular Service* **11880** (2011).

73. Mooley, K. *et al.* GRB 110328A / Swift J164449.3+573451: Followup at 15 GHz. *The Astronomer's Telegram* **3252**, 1 (2011).

74. Zauderer, A. *et al.* The Birth of a Relativistic Outflow in the Unusual γ-ray Transient Swift J164449.3+573451. *Nature,* in press (2011).

75. Aliu, E. *et al.* VERITAS Observations of the Unusual Extragalactic Transient Swift J164449.3+573451. *Astrophys. J.* in press (2011). arXiv:1107.1738.

76. Bloom, J. S. *et al.* A relativistic jetted outburst from a massive black hole fed by a tidally disrupted star. *Science* **333**, 203 (2011). arXiv:1104.3257.

77. Ghisellini, G. *et al.* General physical properties of bright Fermi blazars. *Mon. Not. R. Astron. Soc.* **402**, 497–518 (2010).

78. Ghisellini, G. & Tavecchio, F. Canonical high-power blazars. *Mon. Not. R. Astron. Soc.* **397**, 985–1002 (2009).

79. Ghez, A. M. *et al.* Measuring Distance and Properties of the Milky Way's Central Supermassive Black Hole with Stellar Orbits. *Astrophys. J.* **689**, 1044–1062 (2008).

80. Gillessen, S. *et al.* Monitoring Stellar Orbits Around the Massive Black Hole in the Galactic Center. *Astrophys. J.* **692**, 1075–1109 (2009).

81. Baganoff, F. K. *et al.* Rapid X-ray flaring from the direction of the supermassive black hole at the Galactic Centre. *Nature* **413**, 45–48 (2001).

82. Shcherbakov, R. V. & Baganoff, F. K. Inflow-Outflow Model with Conduction and Self-consistent Feeding for Sgr A*. *Astrophys. J.* **716**, 504–509 (2010).

83. Evans, C. R. & Kochanek, C. S. The tidal disruption of a star by a massive black hole. *Astrophys. J. (Letters)* **346**, L13–L16 (1989).

84. Ulmer, A. Flares from the Tidal Disruption of Stars by Massive Black Holes. *Astrophys. J.* **514**, 180–187 (1999).

85. Bogdanović, T., Eracleous, M., Mahadevan, S., Sigurdsson, S. & Laguna, P. Tidal Disruption of a Star by a Black Hole: Observational Signature. *Astrophys. J.* **610**, 707–721 (2004).

86. Guillochon, J., Ramirez-Ruiz, E., Rosswog, S. & Kasen, D. Three-dimensional Simulations of Tidally Disrupted Solar-type Stars and the Observational Signatures of Shock Breakout. *Astrophys. J.* **705**, 844–853 (2009).

87. Strubbe, L. E. & Quataert, E. Optical flares from the tidal disruption of stars by massive black holes. *Mon. Not. R. Astron. Soc.* **400**, 2070–2084 (2009).

88. Brassart, M. & Luminet, J. Relativistic tidal compressions of a star by a massive black hole. *Astron. Astrophys.* **511**, A80 (2010).

89. Brassart, M. & Luminet, J. Shock waves in tidally compressed stars by massive black holes. *Astron. Astrophys.* **481**, 259–277 (2008).

90. Grindlay, J. E. Hard X-ray Timing with EXIST. In P. Kaaret, F. K. Lamb, & J. H. Swank (ed.) *X-ray Timing 2003: Rossi and Beyond*, vol. 714 of *American Institute of Physics Conference Series*, 413–422 (2004).

91. Donley, J. L., Brandt, W. N., Eracleous, M. & Boller, T. Large-Amplitude X-Ray Outbursts from Galactic Nuclei: A Systematic Survey using ROSAT Archival Data. *Astron. J.* **124**, 1308–1321 (2002).

92. Gezari, S. *et al.* Luminous Thermal Flares from Quiescent Supermassive Black Holes. *Astrophys. J.* **698**, 1367–1379 (2009).

93. Wang, J. & Merritt, D. Revised Rates of Stellar Disruption in Galactic Nuclei. *Astrophys. J.* **600**, 149–161 (2004).

94. Lodato, G., King, A. R. & Pringle, J. E. Stellar disruption by a supermassive black hole: is the light curve really proportional to $t^{-5/3}$? *Mon. Not. R. Astron. Soc.* **392**, 332–340 (2009).

95. Lodato, G. & Rossi, E. M. Multiband light curves of tidal disruption events. *Mon. Not. R. Astron. Soc.* **410**, 359–367 (2011).

96. Krolik, J. H. & Piran, T. Swift J1644+57: A White Dwarf Tidally Disrupted by a 10^4 M_{odot} Black Hole? *Astrophys. J., submitted* (2011). arXiv:1106.0923.